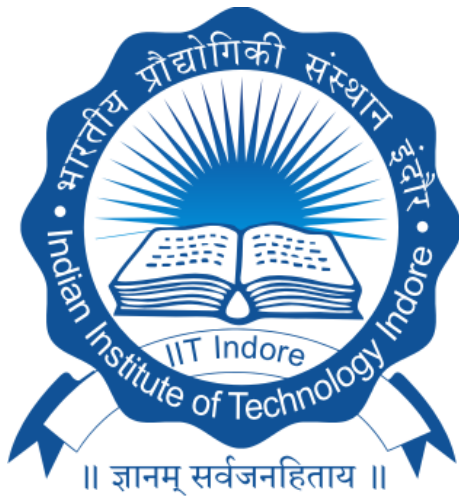


# **CHARACTERISING MAGNETIC RECONNECTION IN ASYMMETRIC MEDIUM**

**M.Sc. Thesis**

**By:**  
**Avinash Kumar Himanshu**



**DEPARTMENT OF ASTRONOMY , ASTROPHYSICS AND  
SPACE ENGINEERING**

**INDIAN INSTITUTE OF TECHNOLOGY  
INDORE**

**April, 2023**

# CHARACTERISING MAGNETIC RECONNECTION IN ASYMMETRIC MEDIUM

A THESIS

*Submitted in partial fulfillment of the  
requirements for the award of the degree  
of  
Master of Science*

*by*  
**Avinash Kumar Himanshu**



**DEPARTMENT OF ASTRONOMY , ASTROPHYSICS AND  
SPACE ENGINEERING**

**INDIAN INSTITUTE OF TECHNOLOGY  
INDORE**

**April, 2023**

# **INDIAN INSTITUTE OF TECHNOLOGY INDORE**

## **CANDIDATE'S DECLARATION**

I hereby certify that the work which is being presented in the thesis entitled "**characterising magnetic reconnection in asymmetric medium**" in the partial fulfillment of the requirements for the award of the degree of MASTER OF SCIENCE and submitted in the DEPARTMENT OF ASTRONOMY , ASTROPHYSICS AND SPACE ENGINEERING , Indian Institute of Technology Indore, is an authentic record of my own work carried out during the time period from July, 2022 to May, 2023 under the supervision of Dr. Bhargav Vaidya . The matter presented in this thesis has not been submitted by me for the award of any other degree of this or any other institute.

Signature with date  
**Avinash Kumar Himanshu**

---

This is to certify that the above statement made by the candidate is correct to the best of my knowledge.

Signature of the Supervisor of  
M.Sc. Thesis  
**DR. BHARGAV VAIDYA**

---

**Avinash Kumar Himanshu** has successfully given his M.Sc. Oral Examination held on .....

Signature(s) of Supervisor(s) of  
MSc thesis, Date:

Convener, DPGC  
Date:-

Signature of PSPC Member 1  
Date:-

Signature of PSPC Member 2  
Date:-

## Abstract

Physically speaking, magnetic reconnection is a cornerstone phenomenon of plasmas. During this process, the magnetic field permeating a conductive plasma rapidly rearranges itself, and releases energy and accelerates particles. Reconnection can take place in a variety of different astrophysical plasma environments as well as in laboratory plasmas. In space plasma, the conditions for reconnections are typically not symmetric on either side of the diffusion region. Previous theoretical studies of the plasmoid instability typically assume symmetric reconnecting magnetic fields. We loosen up this assumption by simulating the plasmoid instability during asymmetric inflow magnetic reconnection in two dimensions three component using kinetic model with the help of a Particle-In-Cell named Smilei ([Derouillat et al., 2018](#)). The study results that are presented here contribute to an advancement in our understanding of the process by which reconnections occur in asymmetrical environments. The investigation focused on analyzing the relationship between the degree of asymmetry and the rate of reconnection, as well as the variation in energy distribution.

# Contents

<b>1</b>	<b>Introduction</b>	<b>1</b>
1.1	Plasma . . . . .	1
1.1.1	Plasma: the fourth state of matter . . . . .	1
1.1.2	Macroscopic Neutrality . . . . .	2
1.1.3	Debye Shielding . . . . .	2
1.1.4	Plasma Frequency . . . . .	2
1.1.5	Plasma in the Nature . . . . .	3
1.2	Magnetic Reconnection . . . . .	3
1.2.1	Physics behind magnetic reconnection . . . . .	6
1.2.2	Sweet-Parker Model: Slow Reconnection . . . . .	6
1.2.3	Petschek Model: Fast Reconnection . . . . .	7
1.3	Different Models for Plasma . . . . .	9
1.3.1	MHD Model . . . . .	9
1.3.2	Two Fluid Model . . . . .	10
1.3.3	Kinetic Model . . . . .	10
1.4	Motivation . . . . .	12
<b>2</b>	<b>Kinetic Plasma Modelling: Particle-In-Cell (PIC)</b>	<b>13</b>
2.1	Overview . . . . .	13
2.2	PIC cycle . . . . .	14
2.2.1	Particle-Mesh . . . . .	14
2.2.2	Integration of the Field Equations . . . . .	17
2.2.3	Force/Field Weighting . . . . .	18
2.2.4	Particle Push . . . . .	19
<b>3</b>	<b>Getting hands on PIC: ePic (1D-Electrostatic PIC)</b>	<b>21</b>
3.1	Interpolator Validation . . . . .	21
3.2	Field Solver validation . . . . .	21
3.3	Particle Pusher Validation . . . . .	23
3.4	Two Stream Instability test: A diagnostic for Electrostatic Particle-In-Cell . . . . .	25

<b>4 Results: Plasmoid Instability in PIC</b>	<b>28</b>
4.1 Smilei: Electromagnetic Particle-In-Cell . . . . .	28
4.1.1 PIC algorithms in Smilei . . . . .	28
4.1.2 Computational cycle . . . . .	29
4.1.3 PIC units . . . . .	30
4.2 Our Setup for the simulation . . . . .	31
4.2.1 Parameters used in input file . . . . .	31
4.2.2 Asymmetric Configurations: Magnetic Field and Density . . . . .	32
4.3 Plasmoid Instability and Reconnection . . . . .	33
4.3.1 Plasmoids formation in our simulated systems for different degree of asymmetry (K) . . . . .	33
4.4 Reconnection Rate . . . . .	38
4.4.1 Reconnection rates of our five simulations . . . . .	38
4.4.2 Average reconnection rates for different simulations .	40
4.5 Energy bifurcation during magnetic reconnection . . . . .	41
4.5.1 Magnetic field energy . . . . .	42
4.5.2 Electric field energy . . . . .	43
4.5.3 Kinetic energy . . . . .	45
<b>5 Summary and Conclusion</b>	<b>47</b>

## BIBLIOGRAPHY

# List of Figures

1.1	various plasma types over the density-temperature plane with logarithmic scale . . . . .	4
1.2	Sketch of earth's magnetosphere showing rectangular-shaped region where magnetic reconnection is most often observed . . . . .	4
1.3	The sketch of Sweet-Parker model of reconnection from collisions between two distinct magnetic domains . . . . .	5
1.4	Illustration of Sweet-Parker model. (Yamada et al., 1999) . . . . .	7
1.5	Structure of the magnetic field in Petschek's solution . . . . .	8
1.6	Kinetic simulation with n-body approach. Dotted line represent the Coulomb interaction. (Konior, 2017) . . . . .	11
1.7	Particle-In-Cell method. Dotted line represent interaction of particle and field on mesh. (Konior, 2017) . . . . .	11
2.1	Schematic Particle-In-Cell computation cycle. (Konior, 2017)	14
2.2	Particle mesh for Particle-in-Cell with particle scattered all over. (N-Body, 2011) . . . . .	15
2.3	Density weighting schemes (Gibbon and Sutmann, 2002): a) NGP, b) CIC and c) TSC. . . . .	16
2.4	Schematic of Cloud-In-Cell algorithm. (Konior, 2017) . . . . .	16
2.5	Five-Point-Stencil for Finite difference solver. . . . .	18
2.6	Schematic of Leapfrog integrator, it shows kick (first upward arrow), drift (downward arrow) and again kick (second upward arrow). (Ahedo et al., 2007) . . . . .	19
2.7	Velocity space depicting rotation from $\mathbf{v}^-$ to $\mathbf{v}^+$ . Projections of the total velocities onto the plane normal to the magnetic field are shown. Birdsall and Langdon (1991) . . . . .	20
3.1	Particle Mesh generated by the script written by us with particle weighting using Cloud-in-Cell interpolation . . . . .	22
3.2	Electric field due to electric dipole obtained with field solver written by us. Red dot represents the positively charged particle and blue dot represent the negatively charged particle.	22

3.3	Path of electron in magnetic field using moved with Boris-Scheme . . . . .	23
3.4	Cyclotron using Runge-Kutta, Leapfrog and Boris-Push . . . . .	24
3.5	Two stream instability (Initial state) . . . . .	26
3.6	Two stream instability (evolved into instability state) . . . . .	26
3.7	Velocity distribution of electron in two streams at initial state ( $t = 0\omega_p^{-1}$ ). Initially all particles are distributed into two part one with velocity of $-3 \times 10^{-5}c$ and another $3 \times 10^{-5}c$	27
3.8	Velocity distribution after $t = 101\omega_p^{-1}$ . The velocity is approaching zero. It should become gaussian with a mean of zero, but due to numerical error and our simulation's insufficient resolution, it is distributed as shown. . . . .	27
4.1	Yee lattice (Derouillat et al., 2018) . . . . .	30
4.2	These images show the evolution of current density in z-direction for $K = 1$ . The lines with arrow show the direction of magnetic field in x-y plane. The image on the top is snapshot at $t = 0\omega_p^{-1}$ , image on the middle is snapshot at $t = 250\omega_p^{-1}$ and the bottom is at $t = 500\omega_p^{-1}$ , here $\omega_p$ is the plasma frequency. . . . .	35
4.3	These images show the evolution of current density in z-direction for $K = 1.5$ . The lines with arrow show the direction of magnetic field in x-y plane. The image on the top is snapshot at $t = 0\omega_p^{-1}$ , image on the middle is snapshot at $t = 250\omega_p^{-1}$ and the bottom is at $t = 500\omega_p^{-1}$ , here $\omega_p$ is the plasma frequency. . . . .	36
4.4	These images show the evolution of current density in z-direction for $K = 2$ . The lines with arrow show the direction of magnetic field in x-y plane. The image on the top is snapshot at $t = 0\omega_p^{-1}$ , image on the middle is snapshot at $t = 250\omega_p^{-1}$ and the bottom is at $t = 500\omega_p^{-1}$ , here $\omega_p$ is the plasma frequency. . . . .	37
4.5	The plot illustrates the variation of reconnection rate over time for five distinct degrees of symmetry. The logarithmic scale is utilized for the y-axis to indicate the magnetic reconnection rate, whereas the x-axis denotes the time ( $\times 10\omega_p^{-1}$ ), here $\omega_p^{-1}$ is plasma frequency. Note that in this plot we have moving average with windows of 3 data points to smoothen the graph a bit. . . . .	39

4.6	Plot of the average reconnection rate ( $E_{rec,avg}$ ) with varying degrees of asymmetry (K), Dots represent the data we obtained from the simulations, and the line represents the curve fitted with the equation $E_{rec,avg} = Ae^{-\alpha K}$ . . . . .	40
4.7	Plot of change in total magnetic field energy ( $\Delta E_B = E_{B,t} - E_{B,0}$ ) of the system with time ( $\times 10\omega_p^{-1}$ ). We have illustrated here the trend for magnetic energy evolution with time for all five degree of asymmetries (K). . . . .	43
4.8	Plot of change in total electric field energy ( $\Delta E_E = E_{E,t} - E_{E,0}$ ) of the system with time ( $\times 10\omega_p^{-1}$ ). We have illustrated here the trend for electric field energy evolution with time for all five degree of asymmetries (K). . . . .	44
4.9	Plot of change in Total kinetic energy ( $\Delta E_K = E_{K,t} - E_{K,0}$ ) of the system with time ( $\times 10\omega_p^{-1}$ ). We have illustrated here the trend for kinetic energy evolution with time for all five degree of asymmetries (K). . . . .	45

# Chapter 1

## Introduction

The primary objective of this project is to investigate the process of plasmoid instability caused by magnetic reconnection in an asymmetric current-sheet system, which is analogous to what is typically discovered in the plasma environments that are characteristic of astrophysical and space environments. We attempted to model the process of magnetic reconnection using the conditions that are found in the magnetosphere of the earth. Let's begin by taking a cursory look at plasma itself before moving on to discuss magnetic reconnection and plasmoid instability in more depth.

### 1.1 Plasma

Plasma is the common term for the range of substances that are neutral on macroscopic scales but are made up of ions and electrons, which as a result of long-range Coulomb forces display collective behaviour. Plasmas can be found in a variety of different forms. Greek originally used the word "plasma" to describe something that had been shaped. In 1929, Tonks and Langmuir were the first people to apply it to ionised gas created in a tube by an electric discharge, with the ionised gas continuing to maintain its electrical neutrality on long range scale.

#### 1.1.1 Plasma: the fourth state of matter

The strength of the intermolecular forces of attraction that hold solids, liquids, and gases together is what distinguishes them fundamentally from each other. These forces of adhesion are comparatively strong in solids, weak in liquids, and essentially nonexistent in gases. A substance's temperature, or the thermal energy (random kinetic energy) of its molecules (or atoms), determines which of these states it is found in. The state is determined by the equilibrium between the particles kinetic energy and their inter-particle forces.

The atoms and molecules within a substance gain thermal kinetic energy as the temperature of the substance rises, eventually becoming more energetic than the binding potential energy and breaking free of the substance, resulting in phase transitions under constant pressure and temperature. When enough energy is introduced into the system, the molecular gas dissociates into atomic gas due to the collision of particles with enough energy to break the molecular bond. Furthermore, if enough energy is applied, the electrons in the atom's outermost orbits will escape, ionising the gas or turning it into plasma.

This transition into plasma from a gas, however, is not a thermodynamic phase transition due to the fact that it happens gradually as the temperature rises. Its temperature is determined by the thermal energy (kinetic energy) of its molecules or atoms. The state is determined by the balance between the kinetic energy of each particle and the force of attraction between them.

### 1.1.2 Macroscopic Neutrality

If there is no any external disturbance, a plasma maintains a state of neutrality on a macroscopic scale. Since no external forces are acting on the plasma, the net electric charge in bulk of the plasma large enough to contain a significant number of particles but small enough to be affected by variations in macroscopic parameters like density and temperature is zero under these conditions of equilibrium. There is no net space charge over a macroscopic region because the microscopic charge density fields cancel out one another in the interior of the plasma. The potential energy of the resulting coulomb forces, if this macroscopic neutrality is not held, could be vast compared to the thermal particle kinetic energy. Macroscopic neutrality plays a crucial role in the unique behavior of plasmas, as it enables them to respond collectively to electromagnetic forces, distinguishing them from neutral gases.

### 1.1.3 Debye Shielding

When describing plasmas, the Debye length is an essential physical parameter. It defines how far other charged particles in a plasma travel before feeling the effects of a single charged particle's electric field (or of a surface with a nonzero potential). The charged particles form a shield against electrostatic fields of any scale smaller than the Debye length. Plasma particles act as a shield against electrostatic fields due to their collective interactions. Debye length  $\lambda_D$  is given by Eq.1.1.

$$\lambda_D = \left( \frac{\epsilon_0 k_b T}{n_e e^2} \right)^{1/2} \quad (1.1)$$

where  $\epsilon_0$  is the vacuum permittivity,  $k_b$  is the Boltzmann constant,  $T$  is the electron temperature,  $n_e$  is the electron density, and  $e$  is the elementary charge. Debye shielding helps maintain the overall charge neutrality within the plasma and allows it to behave as a quasi-neutral medium.

### 1.1.4 Plasma Frequency

Plasma exhibits macroscopic neutrality, which is a very important property. One of plasma's most distinguishing features is the remarkable stability of the charge neutrality of its macroscopic space. A plasma's internal space charge fields that result when it is abruptly disturbed from equilibrium cause motions of the particles as a group that aim to reestablish the plasma's original electrical neutrality. The plasma frequency, a naturally occurring oscillation frequency, is what gives rise to these collective motions. The ions' heavy mass prevents them to some extent from following the motion of the electrons because the frequency of these oscillations is extremely high. The ion-electron Coulomb attraction provides the necessary collective restoring force for the electrons to oscillate collectively around the heavy ions. The period of this characteristic oscillation provides

a useful time scale against which to evaluate the effectiveness of dissipative mechanisms designed to halt the collective motions of electrons. The Eq. 1.2 describes the frequencies of electron plasma.

$$\omega_{pe} = \left( \frac{n_e e^2}{m_e \epsilon_0} \right)^{1/2} \quad (1.2)$$

### 1.1.5 Plasma in the Nature

Plasma is abundant in nature and can be found in various forms, ranging from astronomical to terrestrial environments. Some examples of natural plasmas include:

- The solar corona and solar wind: The outer layer of the Sun, known as the solar corona, is a hot, ionized plasma. The solar wind, which is a stream of charged particles ejected from the solar corona, expands outwards and interacts with the Earth's magnetosphere.
- Interstellar medium: The space between stars in a galaxy is filled with a diffuse plasma known as the interstellar medium, composed of ionized gas and dust particles.
- Earth's ionosphere: The ionosphere is a layer of plasma that is present in the uppermost part of the Earth's atmosphere. It is important for radio waves to travel and for satellites to talk to each other.
- Lightning and auroras: Lightning is a plasma discharge that occurs in the Earth's atmosphere, while auroras are natural light displays caused by the interaction between solar wind particles and the Earth's magnetosphere.

Plasmas are also created and controlled in laboratory settings for various applications, such as fusion energy research, plasma processing, and plasma propulsion.

## 1.2 Magnetic Reconnection

The process of magnetic reconnection is inherent in both astrophysical plasmas and laboratory plasmas. In this process, magnetic energy is transformed into the kinetic and fast particle energy by altering the connectivity of magnetic field lines. For instance, it is generally agreed upon that magnetic reconnection plays an important part in both the observed rapid release of energy and the associated particle acceleration that occurs during solar flares ([Priest and Forbes, 2000a](#)).

Reconnection serves as the catalyst for numerous impressive events within the solar system. For example, magnetic reconnection is believed to be the energy source for solar flares occurring near sunspots. Solar magnetic activity, including flares, can propel high-energy charged particles into space. Upon reaching Earth, these particles can disrupt communication and power systems, pose risks to satellites, and harm spacecraft. The solar wind, resulting from the sun's magnetic field, constantly affects Earth's magnetic field. During intense bursts (such as those caused by extraordinary solar flares), reconnection can take place in the near-Earth magnetotail (a slender magnetic field structure on the night side, several Earth-radii away). The thin plasma in this region is once again

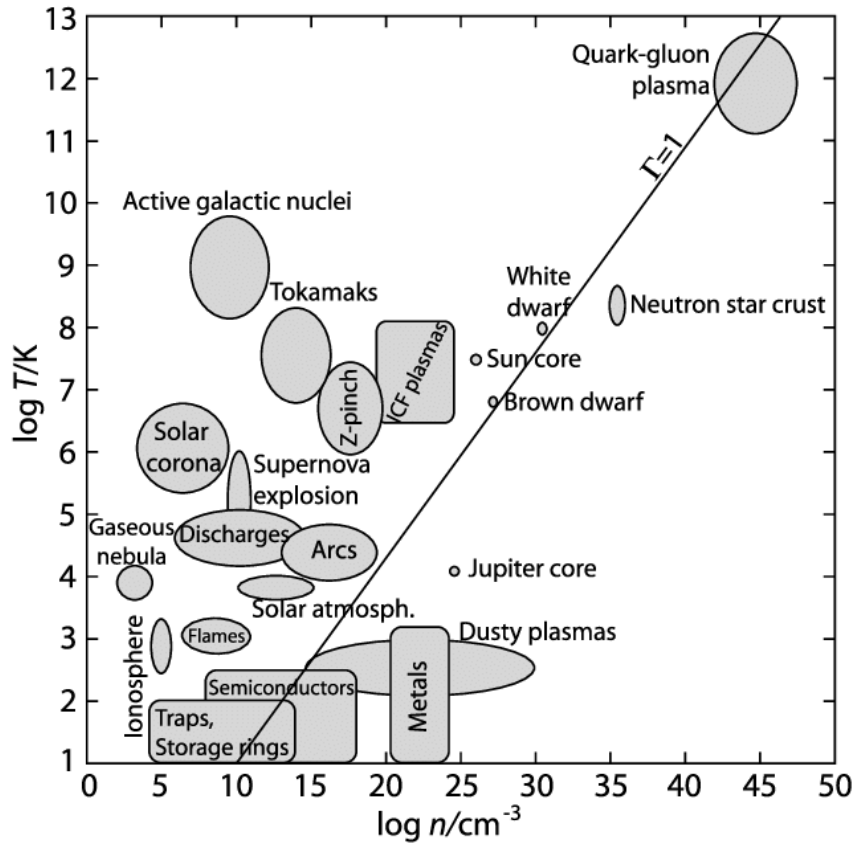


Figure 1.1: various plasma types over the density-temperature plane. Take note of the extraordinarily broad range of these parameters. Right off the  $\Gamma = 1$  line are strongly coupled plasmas. The ratio of potential to kinetic energy is represented by the symbol  $\Gamma$ . ([Donkó et al., 2007](#))

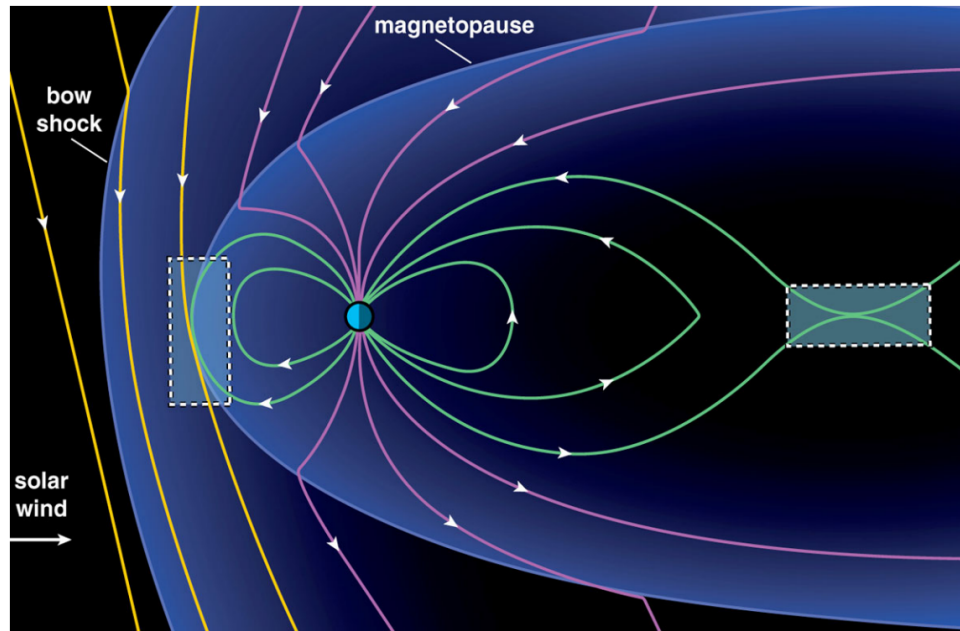


Figure 1.2: The rectangular area of the earth's magnetosphere shown in the sketch is where magnetic reconnection is most frequently seen. ([Bathgate et al., 2018](#))

pushed into the polar areas by magnetic field lines, where it interacts with Earth's atmosphere, exciting nitrogen, oxygen atoms, and other atoms already present. As these atoms de-excite rapidly, the aurora, also known as the northern (and southern) lights, is generated, showcasing a visually stunning and often intricate light display.

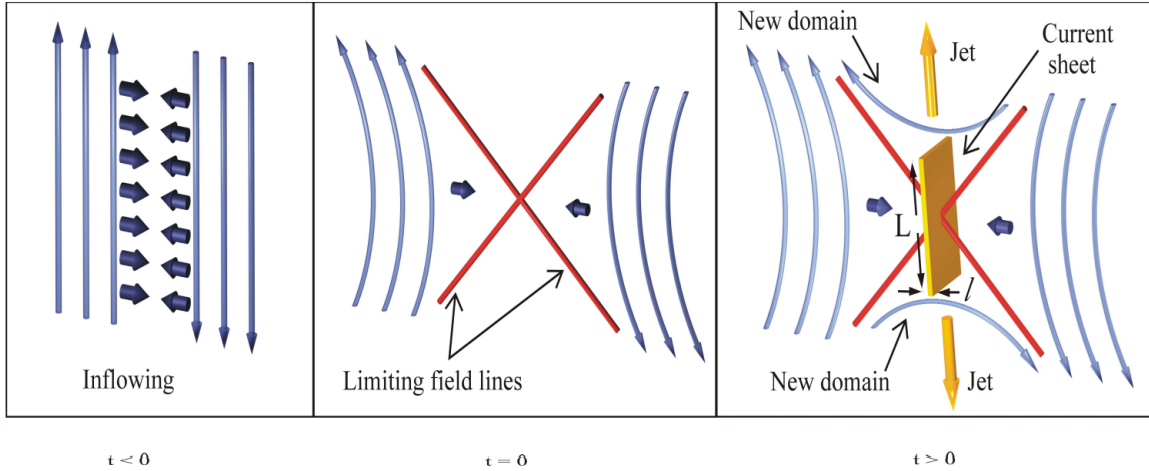


Figure 1.3: “The Sweet–Parker model of reconnection proposes that collisions between two separate magnetic domains in plasma produce plasma jets by reconnection of magnetic field lines in a current sheet or diffusion region that forms between the domains. At  $t < 0$ , inflowing plasma with embedded magnetic flux initiates the process. At  $t = 0$ , an X-type magnetic null is produced by the interaction of opposing magnetic field lines. The limiting field lines are known as separatrices and form an “X” from which the term “X”-type null point is derived. At  $t > 0$  a current sheet forms a diffusion region, jets of heated plasma are ejected from the current sheet, lines of force are broken and rejoined, and four separate magnetic domains are created” ([Bathgate et al., 2018](#))

Because solar wind plasma and solar energetic particles (SEPs) are being drawn into the magnetosphere of the Earth as a result of the process of magnetic reconnection, this phenomenon also has direct repercussions for our home planet. On the surface of the sun, reconnections are what give rise to the generation of these particles. In the context of magnetic reconnection, two problems that continue to arise are the division of magnetic energy that occurs during the process of energy conversion and the production of high-energy particles by non-thermal acceleration mechanisms that are located in close proximity to the reconnection sites.

Almost everywhere there is plasma, a process known as magnetic reconnection takes place. Magnetic reconnection is quite common because stars and the vast majority of the visible universe are made of plasma. It is not well understood, though.

Magnetic reconnection can be modeled in a variety of different ways. The Sweet-Parker model, the Petschek model, stochastic reconnection, and collisionless reconnection are some of the most well-known and widely accepted models.

### 1.2.1 Physics behind magnetic reconnection

The generalised version of Ohm's law is able to adequately describe the dissipative processes that take place in the diffusion region.

$$\mathbf{E} + \mathbf{v} \times \mathbf{B} = \eta \mathbf{J} + \frac{\mathbf{J} \times \mathbf{B}}{en} + \frac{\nabla \cdot \tilde{\mathbf{P}}_e}{en} + \frac{m_e}{e} \frac{d\mathbf{v}_e}{dt} \quad (1.3)$$

In Eq.4.8,  $\mathbf{E}$  and  $\mathbf{B}$  electric and magnetic field vector respectively,  $\eta$  is anomalous resistivity,  $\mathbf{J}$  is current vector,  $P_e$  is electron pressure tensor,  $\mathbf{v}$  is the plasma velocity,  $n$  is plasma density and  $m_e$  is mass of electron. For ideal MHD right side of Eq:4.8 must be zero, but if any of the term in right hand side is not zero then it will violate the ideal MHD and reconnection will occur. In the generalised form of Ohm's law each term on right side of Eq.4.8 represent specific physical phenomena.

**Anomalous Resistivity ( $\mathbf{E} = \eta \mathbf{J}$ ):** If wave turbulence produces an anomalous resistivity  $\eta$ , ohmic dissipation can occur in a current-carrying collisionless plasma. According to Parker's description, the inflow and outflow of a reconnection diffusion region driven by Alfvén waves can cause the magnetic field's energy to be dissipated within the region due to this inherent resistivity([Parker, 1957](#)).

**Hall-MHD ( $\mathbf{E} = \mathbf{J} \times \mathbf{B}/en$ ):** As ions and electrons move relative to one another under the influence of the Lorentz force, currents are generated and propagate through the diffusion region, generating a quadrupolar magnetic field component that is normal to the plane of reconnection. ([Lui et al., 2005](#)). Huba has outlined the basics of this tweak to MHD ([Huba, 1995](#)), who emphasises the significance of it to plasma dynamics taking place on length scales that are shorter than an ion inertial length ( $c/\omega_{pi}$ ), where  $c$  being light's velocity and  $\omega_{pi}$  the ion plasma frequency, and time scales shorter than an ion cyclotron period. In the lab and in space, Hall-MHD predictions for reconnection have been validated ([Ren et al., 2005](#)), ([Borg et al., 2005](#)).

**Divergence of Electron Pressure Tensor  $\mathbf{E} = \nabla \cdot \tilde{\mathbf{P}}_e/en$  :** When the electron pressure tensor divergence is present, ambipolar electric fields and kinetic Alfvé waves are produced, and the reconnection mechanism shifts from being driven by Alfvén waves to being driven by the whistler mode([Mandt et al., 1994](#)).

**Electron Inertia Effects ( $(m_e/e)d\mathbf{v}_e/dt$ ):** Relative motion between electrons and the magnetic field is thought to be responsible for thermal electrons' non-instantaneous response to electric field fluctuations, which may be caused by Langmuir oscillations or other wave-particle interactions at the smaller plasma scales. At these length scales, the differential motion of electrons causes kinetic Alfvén waves to decay into inertial Alfvén waves and be destroyed. The electric field that is parallel to  $\mathbf{B}$ , that is one of the components of the electric field that is produced by reconnection, is one of the significant outcomes of this dissipation.

### 1.2.2 Sweet-Parker Model: Slow Reconnection

Important to the Sweet-Parker model, as depicted in Fig. 1.4, is the presence of a "diffusion region," which is primarily a rectangular area in which the magnetic field diffuses and reconnects. The size of such a area is crucial because it controls the speed

of magnetic reconnection by balancing the flow of plasma and flux into and out of the region, and it also sets the time scale for reconnection. This box's width is affected by the regional plasma resistivity that accelerates magnetic diffusion, so higher resistivities lead to greater reconnection rates. The length of this box is on a macroscopic scale ([Yamada et al., 1999](#)).

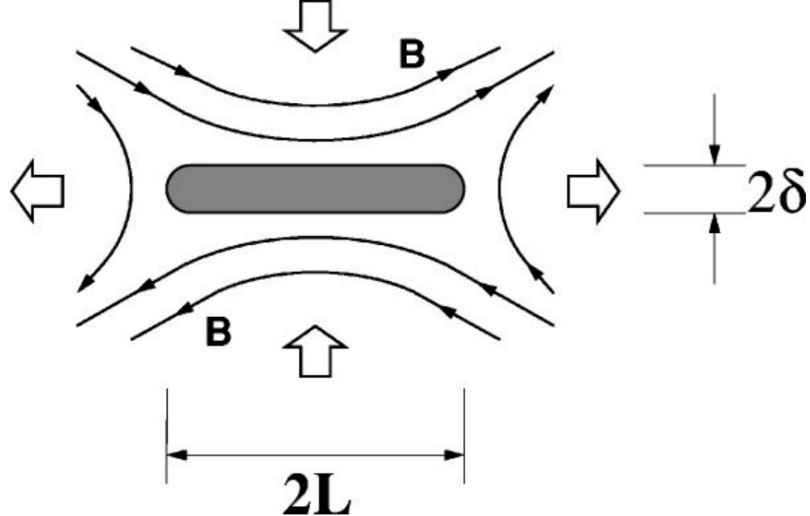


Figure 1.4: Illustration of Sweet-Parker model. ([Yamada et al., 1999](#))

In a MHD plasma with resistivity  $\eta$  the motion of magnetic field is described by Eq.1.4.

$$\frac{\partial \mathbf{B}}{\partial t} = \nabla \times (\mathbf{V} \times \mathbf{B}) + \frac{\eta}{\mu_0} \nabla^2 \mathbf{B} \quad (1.4)$$

where  $\mathbf{V}$  is the flow velocity. On the right hand side the first term represent the effect of plasma convection with time scale of Alfvén time  $\tau = L/\mathbf{V}_A$  (where,  $L$  is diffusion region and  $\mathbf{V}_A = \mathbf{B}/\sqrt{\mu_0 \rho}$  is Alfvén speed). The second term define the field line diffusion, whose time scale is diffusion time,  $\tau_R = \mu_0 L^2 / \eta$ . The relative importance of magnetic diffusion to plasma convection is given by  $\tau_R / \tau_A = \mu_0 L \mathbf{V}_A / \eta$ .

### 1.2.3 Petschek Model: Fast Reconnection

In 1964, Petschek's advanced adaptation of the Sweet-Parker model in a narrow current sheet significantly progressed the field. Both Sweet and Parker made the same assumption that the length of the current sheet is equal to the global field's scale size,  $L_e$ . In their solution, the Alfvén Mach number,  $M_{Ae}$ , of the plasma inflow into the sheet is related to the Reynolds number ( $R_{me}$ ) by Eq. 1.5:

$$M_{Ae} = R_{me}^{-1/2} \text{ where, } R_{me} = L_e \mathbf{V}_{Ae} / \eta \quad (1.5)$$

where  $\mathbf{V}_{Ae}$  denotes the Alfvén speed in the inflow region, and  $\eta$  represents the plasma diffusivity. Sweet-Parker reconnection is extremely slow ( $M_{Ae} \approx 10^{-3}$  to  $10^{-6}$ ) compared to the rates needed to account for the rapid release of magnetic energy observed in events such as solar flares and magnetospheric substorms ( $M_{Ae} \approx 0.1$ ), because in typical astrophysical plasmas,  $R_{me}$  generally ranges from  $10^6$  to  $10^{12}$ .

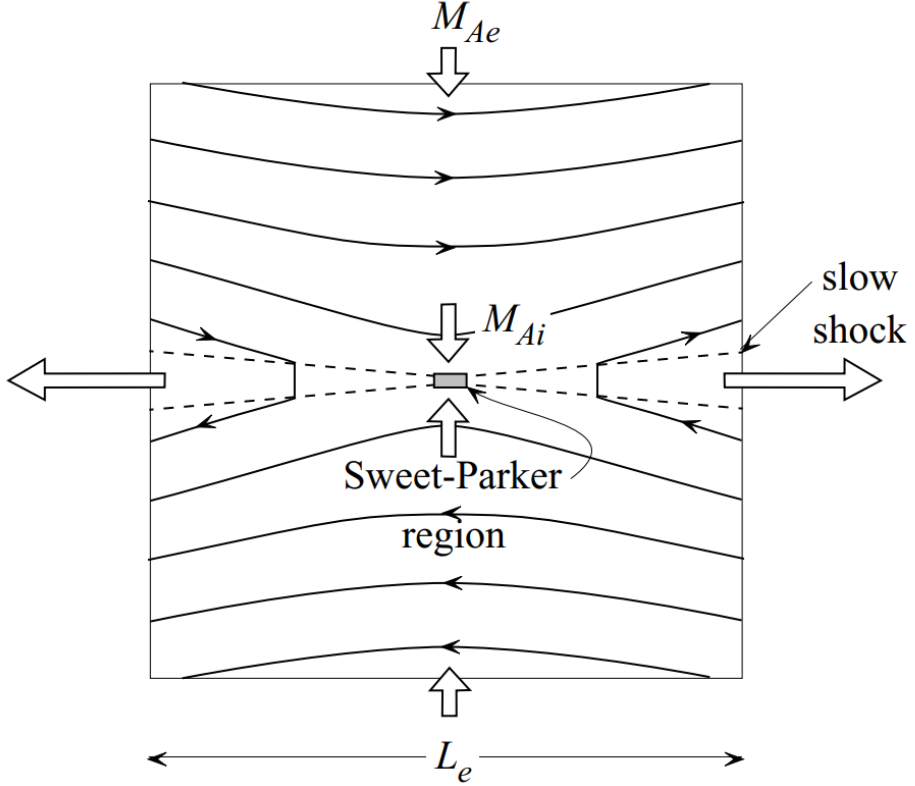


Figure 1.5: Petschek’s solution displays a well-ordered magnetic field arrangement. The small rectangle at the center of the image represents the brief current sheet for the Sweet-Parker region. The dashed lines illustrate the four slow-mode shocks that emerge from this area.  $M_{Ae}$  and  $M_{Ai}$  represent the inflow Alfvén Mach numbers at the outer and inner boundaries of the external region surrounding the Sweet-Parker zone, respectively. (Forbes, 2001)

Petschek proposed a faster reconnection rate by surrounding the Sweet-Parker region with an external magnetic field, causing the current sheet’s length  $L$  to be significantly smaller than the global scale length  $L_e$ . In Petschek’s configuration, the diffusion region current sheet is confined to a small central area, with the majority of the magnetic field energy being converted into heat and bulk kinetic energy. This conversion occurs at four stationary slow-mode shocks connected to the corners of the diffusion region, as illustrated in Fig. 1.5. Petschek also assumed an inflow region free of current in the magnetic field. This assumption, together with the trapezoidal shape of the inflow region formed by the slow shocks, leads to a logarithmic decrease in the magnetic field as the inflowing plasma approaches the Sweet-Parker current sheet. The maximum reconnection rate provided by Petschek is expressed in Eq. 1.6

$$M_{Ae} = \pi / (8 \ln R_{me}) \quad (1.6)$$

where  $R_{me}$  is the magnetic Reynolds number. According to this model, the reconnection rates are an order of magnitude higher than those of the Sweet-Parker model due to their logarithmic dependence on  $R_{me}$ . Petschek’s formula yields  $M_{Ae} \approx 10^{-1}$  to  $10^{-2}$  for laboratory applications and most space reconnections.

The typical reconnection rate predicted by the Sweet-Parker model is:

$$M_A \sim S^{-1/2} \quad (1.7)$$

Where as the same predicted by the Petschek model is:

$$M_A \sim \ln(S) \quad (1.8)$$

where  $S$  is Lundquist number and  $M_A$  is the Alfvén Mach number, a dimensionless parameter that measures the reconnection rate. For high Lundquist number plasmas, the Sweet-Parker model predicts a very slow reconnection rate, which is not consistent with observations of fast reconnection events in space and laboratory plasmas.

## 1.3 Different Models for Plasma

Due to the multiscale nature of plasma, we can model plasma in the following ways:

- Fluid (Magneto-hydrodynamic - MHD) Model
- Two fluid
- Particle (Kinetic) Model

### 1.3.1 MHD Model

Plasma is regarded as a single fluid in the ideal MHD model. Plasma is regarded as an electrically conducting fluid in the magnetohydrodynamic model. The governing equations are fluid dynamics equations and Maxwell's equations. A self-consistent set of MHD equations connects the plasma mass density  $\rho$ , plasma velocity  $\mathbf{V}$ , thermodynamic pressure  $P$ , and magnetic field  $\mathbf{B}$ . In order to derive MHD strictly, Ignore electron motion and only take into account heavier ions.

The first equation is mass conservation.

$$\frac{\partial \rho}{\partial t} + \nabla(\rho \mathbf{V}) = 0 \quad (1.9)$$

Second equation is equation of motion of a fluid element,

$$\rho \left[ \frac{\partial \mathbf{V}}{\partial t} + (\mathbf{V} \nabla) \mathbf{V} \right] = -\nabla P + \mathbf{j} \times \mathbf{B} \quad (1.10)$$

It is Euler equation. The density of the electric current is denoted by the vector  $\mathbf{j}$ , and it can be expressed using the magnetic field  $\mathbf{B}$ .

Next is the energy equation, which has the following form in the most basic adiabatic case.

$$\frac{d}{dt} \left( \frac{P}{\rho^\gamma} \right) = 0 \quad (1.11)$$

where  $\gamma$  is the specific heats ratio i.e  $C_p/C_V$ .

Fourth equation is induction equation.

$$\frac{\partial \mathbf{B}}{\partial t} = \nabla \times (\mathbf{V} \times \mathbf{B}) \quad (1.12)$$

The MHD plasma model is used to study plasma on a large scale. It should be used to study plasma with collision at scale length greater than the mean free path of collision. Although it functions well in the system, if its length scale is greater than the gyroradius of the ions contained within it.

### 1.3.2 Two Fluid Model

Ohm's law, which is used to approximate the current density in a conducting fluid, does not produce a desirable result in the case of a plasma. In the two-fluid model two different fluids ions and electrons, provides a more thorough explanation of the electric currents in a plasma. Contrary to the more precise physical kinetics description, each of these species' motion is characterised by the common equations of hydrodynamics, also known as the hydrodynamic approximation.

We can get more results, some of them complex, using the two-fluid model. Not all of these, however, are accurate due to the approximation's hydrodynamic's errors. We will restrict our analysis to a few straightforward and solid cases ([Frank-Kamenetskii, 1972](#)).

The assumption underlying this model is that all electrons and ions in a given location travel at equal velocity,  $\mathbf{v}_e$  and  $\mathbf{v}_i$ , respectively (ordered of velocities; the correct treatment of thermal motion calls for the use of physical kinetics.). The mass velocity can be defined easily as given in Eq. [1.13](#)

$$\mathbf{v} = \frac{M\mathbf{v}_i + m\mathbf{v}_e}{M + m} \approx \mathbf{v}_i \quad (1.13)$$

where  $M$  is the mass of ions and  $m_e$  is mass of electron. The relative velocity is given by as:

$$\mathbf{v}_i - \mathbf{v}_e \approx \mathbf{v} - \mathbf{v}_e \quad (1.14)$$

this is related to current density as

$$j = Zn_i\mathbf{v}_i - en_e\mathbf{v}_e, \quad (1.15)$$

where  $Z$  is the atomic number of ion and  $e$  is charge on electron.

Because the space charge would otherwise result in a huge electric field, To a minimum, the gap between the ion and electron charges must exist. Consequently, electrical neutrality is a condition.

$$Zn_i \approx n_e \approx n \text{ and therefore, } j = ne(\mathbf{v}_i - \mathbf{v}_e) \quad (1.16)$$

Two fluid model is used in the system where length scale are greater than electron's gyroradius.

### 1.3.3 Kinetic Model

Plasma can also be studied by examining all of its particles and their interactions with one another. In this model, plasma is viewed as a collection of electrons, protons, and ions, and their interactions are investigated. We can simply solve the electromagnetic force between each pair and investigate the plasma. Isn't that the case? Yes, but it's not that simple. Kinetic model be applied on the system with length scale greater than

Debye length.

Modeling the motion of individual particles in a plasma, is a tedious job. For a very simple scenario two charged particles within a plasma interact via Coulomb force given by  $\mathbf{F} = \frac{1}{4\pi\epsilon_0} \frac{q_1 q_2}{r^3} \mathbf{r}_{12}$  within a typical Debye scale. However, a typical plasma system generally consists of millions of particles, requiring a trillion operations (it is a  $n^2$  problem) at each time step. Which is nearly impossible with today's computing technology. This problem, however, can be solved by employing another well-known kinetic modelling of plasma technique, Particle-In-Cell. In Particle-In-Cell technique the concept of a "macro-particle" is used to represent a collection of real ions/electrons. These particles are then dispersed on a grid, and electromagnetic interaction is solved over the grid as well as shown in Fig. 1.6 and 1.7.

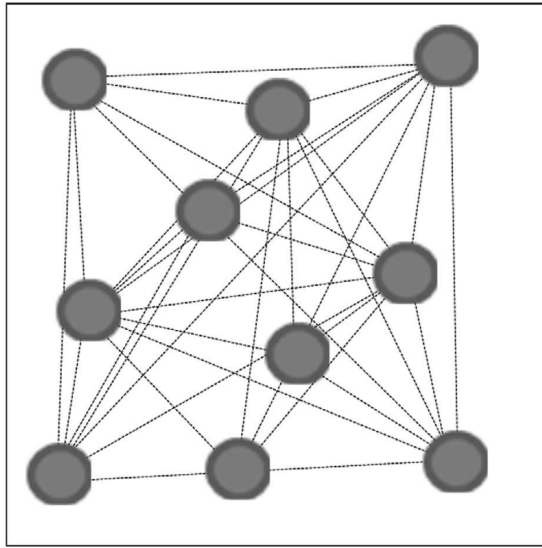


Figure 1.6: Kinetic simulation with n-body approach. Dotted line represent the Coulomb interaction. ([Konior, 2017](#))

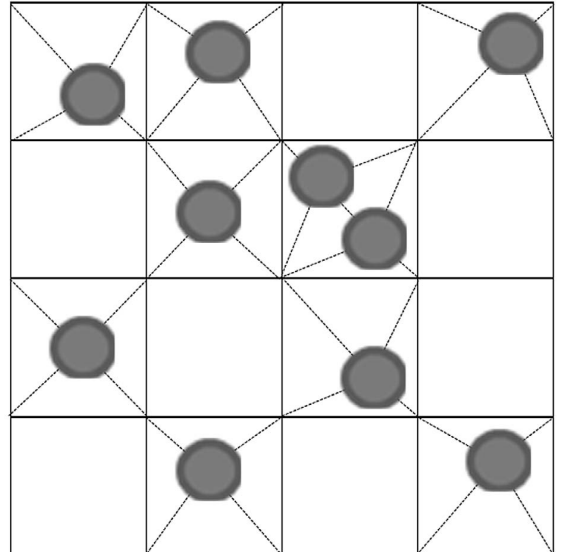


Figure 1.7: Particle-In-Cell method. Dotted line represent interaction of particle and field on mesh. ([Konior, 2017](#))

In kinetic modeling of collisionless plasma people use Vlasov-Maxwell systems of equations. Different species of particle that constitutes the plasma have their describing distribution function  $f_s(t, \mathbf{x}, \mathbf{p})$ , where  $s$  denotes the given species with mass  $m_s$  and charge  $q_s$ ,  $\mathbf{x}$  is position and  $\mathbf{p}$  denotes the momentum. Vlasov's equation is given by the Eq. 1.17

$$\left( \partial_t + \frac{\mathbf{p}}{m_s \gamma} \cdot \nabla + \mathbf{F}_L \cdot \nabla_p \right) f_s = 0 \quad (1.17)$$

where,  $\gamma = (1 + \mathbf{p}^2/m_s^2)^{1/2}$  is Lorentz factor and  $\mathbf{F}_L$  is Lorentz Force (Eq. 2.9). This force is consequence of presence of macroscopic electric and magnetic field, that satisfy the Maxwell's equation (1.18).

$$\nabla \cdot \mathbf{B} = 0 \quad (1.18a)$$

$$\nabla \cdot \mathbf{E} = \rho \quad (1.18b)$$

$$\nabla \times \mathbf{B} = \mathbf{J} + \partial_t \mathbf{E} \quad (1.18c)$$

$$\nabla \times \mathbf{E} = -\partial_t \mathbf{B} \quad (1.18d)$$

**Why using kinetic model for this project?** We intend to study magnetic reconnection by modelling a collisionless asymmetric system. When the length scale is larger than the ion's gyroradius, we use MHD modelling, and when the length scale is larger than the electron's gyroradius, we use two-fluid modelling. However, both MHD and two-fluid models cannot be used for systems with length scales smaller than the electron's gyro-radius; this is where the kinetic model shines, as it can resolve systems with lengths up to debye length. We could also use a kinetic model to track how energy is transferred to particles during magnetic reconnection when the magnetic field is broken.

## 1.4 Motivation

The goal of our project is to investigate magnetic reconnection in an asymmetric medium. In order to investigate the reconnection, we made use of a kinetic plasma model, more specifically the Particle-In-Cell code. However, in order to acquire an in-depth comprehension of the physics that lies behind the kinetic modelling of plasma, we attempted to write our very own simple electrostatic Particle-In-Cell model. Once we reached a point where we had a sufficient understanding of kinetic modelling, we upgraded from our basic electrostatic Particle-In-Cell to an already built advanced electromagnetic Particle-In-Cell named Smilei.

During this project we will be studying about the growth rate of modes of perturbation and global growth. We will also vary some parameters and study its effect on the rate of reconnection.

# Chapter 2

## Kinetic Plasma Modelling: Particle-In-Cell (PIC)

### 2.1 Overview

Particle models are among the most effective models for computer simulations of plasma. By tracking the movement of collections of charged particles in electromagnetic field created by them, one can simulate nature in these models. Although this approach appears straightforward and simple, practical computational constraints necessarily require the use of complex methods. The inability to follow the motion of enough number of particles is the main cause of this need. The motion of more than a few million particles cannot be tracked for a significant amount of time by even the most advanced computers. This can be contrasted with the enormous amount of particles found in both laboratory and natural plasma. That's why, it's possible to interpret each particle in a simulation as being equivalent to collection of actual particles in a plasma (also called quasiparticle or macroparticle). Alternately, The simulation can be seen as a model of a very tiny but typical region of a plasma, for example.

There is a wide variety of particle models that can be used to describe plasma. There are models with one dimension, two dimensions, and three dimensions. There are also electromagnetic, electrostatic, and magnetostatic models.

Plasma can be thought of as an ensemble of particles, each of which possesses a charge, a mass, and a momentum of their own. In this method, the values of electric and magnetic fields are defined over a spatial grid (by solving Maxwell's equation), and then the Lorentz force is utilised to move the macro-particles around. The following procedures, as depicted in the figure, make up a standard implementation of the Particle-In-Cell algorithm (Fig.2.1):

1. Particle Mesh: Distribute the particles over a computational grid and interpolate their charge density over the grid points. (Interpolation was performed using the cloud-in-cell (CIC) technique for this simulation.)
2. Integration of field equations: Calculate the electric and magnetic fields over the spatial grid by solving the Maxwell's equations.
3. Field/Force Weighting: Interpolate the force from the spatial grid to the particle

position.

4. Particle push: Update the particle's position and velocity as per the Lorentz force. (For this simulation, we have used Inverse CIC to interpolate the force back to the particle and the Boris-Pusher technique to move the particle under electromagnetic force.)
5. Repeat: Repeat all the above processes again.

## 2.2 PIC cycle

Each of the steps mentioned above will be thoroughly examined in this chapter.

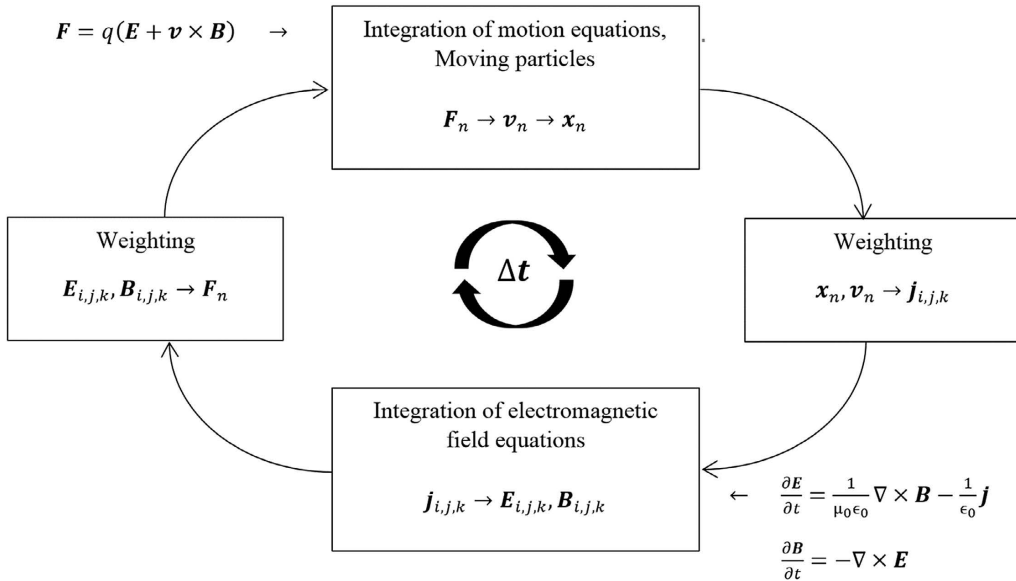


Figure 2.1: Schematic Particle-In-Cell computation cycle. ([Konior, 2017](#))

First, particles are dispersed across the grid, then the system of Maxwell's equations (For electrostatic PIC, only Poisson Equation) are solved to get the electromagnetic field on the grid is, and finally, the electric forces are translated onto the particles. In the final step, we move the particle in accordance with the equation of motion. Let's break down each of the steps and go over them in depth one by one.

### 2.2.1 Particle-Mesh

During the initial stage of Particle-In-Cell simulation, domain is divided up into a spatial grid. Particles are then dispersed across the grid. The fields caused by the particles are interpolated to the closest grid point using the appropriate interpolation techniques. It should be mentioned that the grid resolution must be sufficient to support the necessary plasma simulation. Although the outcome is better with higher grid resolution, the cost is horrendous. The amount of processing power required increases with grid resolution.

The PIC method simultaneously computes moments of the distribution (such as currents and densities) on grid points, but tracks individual particles (or fluid elements) in a continuous phase space [3.1](#). Regardless of how complex the flow is, the particles are

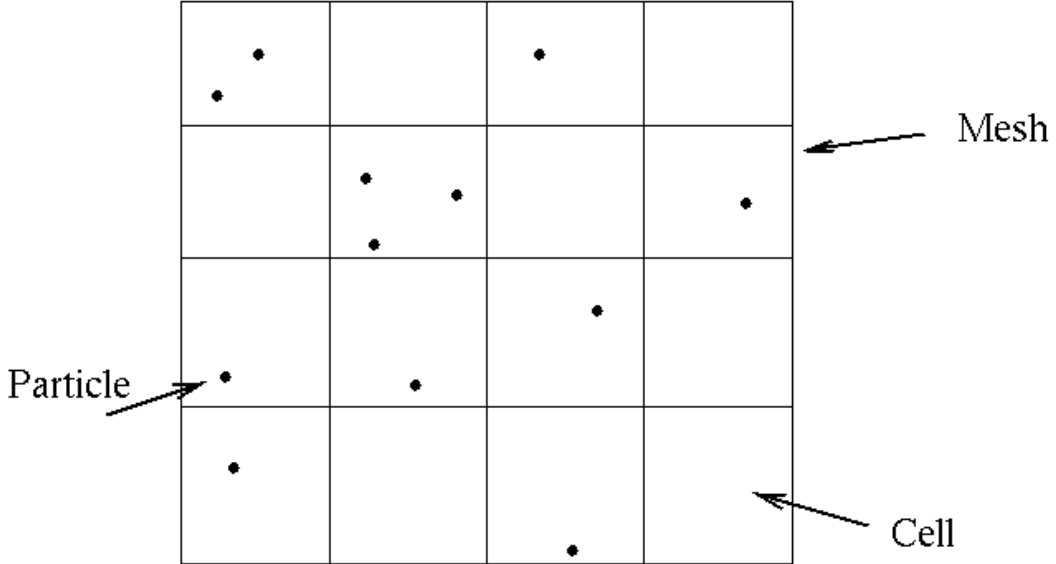


Figure 2.2: Particle mesh for Particle-in-Cell with particle scattered all over. ([N-Body, 2011](#))

free to move and follow its dynamics because they have one or more assigned properties (such as charge, velocity, mass, etc.).

The particle's charge density or current density can be extrapolated over the grid in one of three ways:

- Nearest-Grid-Point (NGP)
- Cloud-In-Cell (CIC)
- Triangular-Shaped-Cloud (TSC)

A zeroth-order interpolation method known as nearest-grid-point, which interpolate all of weight of the particle to the grid in which it is present, regardless of where it is located within the grid. Then there is the Cloud-In-Cell method, a first-order interpolation method that distributes the particle's weight to the grid corners in accordance with the distance between that point and the particle. Because it strikes a good balance between accuracy and computational requirements, CIC is a widely used interpolation technique. The most precise of the three, a second-order triangular-shaped cloud, comes in last (TSC). Comparing all three, TSC requires the most computation.

### Cloud-In-Cell:

The Cloud-in-Cell, or CIC, assignment method is the one that is utilised the most frequently. This method applies multilinear interpolation to the eight grid points that define the cubical mesh cell that is home to the particle (in 3D). This procedure treats each particle as if it were a cubic cloud with a density that is constant throughout. The following is a concise report on the Cloud-in-Cell method when applied in two dimensions. Consider a particle mesh with each grid corners represented by  $(x_i, y_j)$  and let's consider that spatial resolution (separation of two nodes) is  $\Delta x$  in  $x$ -direction and  $\Delta y$  in  $y$ -direction. Now consider that our particle is located at point  $(x, y)$ , then the weight of this particle will transfer on the 4 nearest node according to Eq. 2.1.

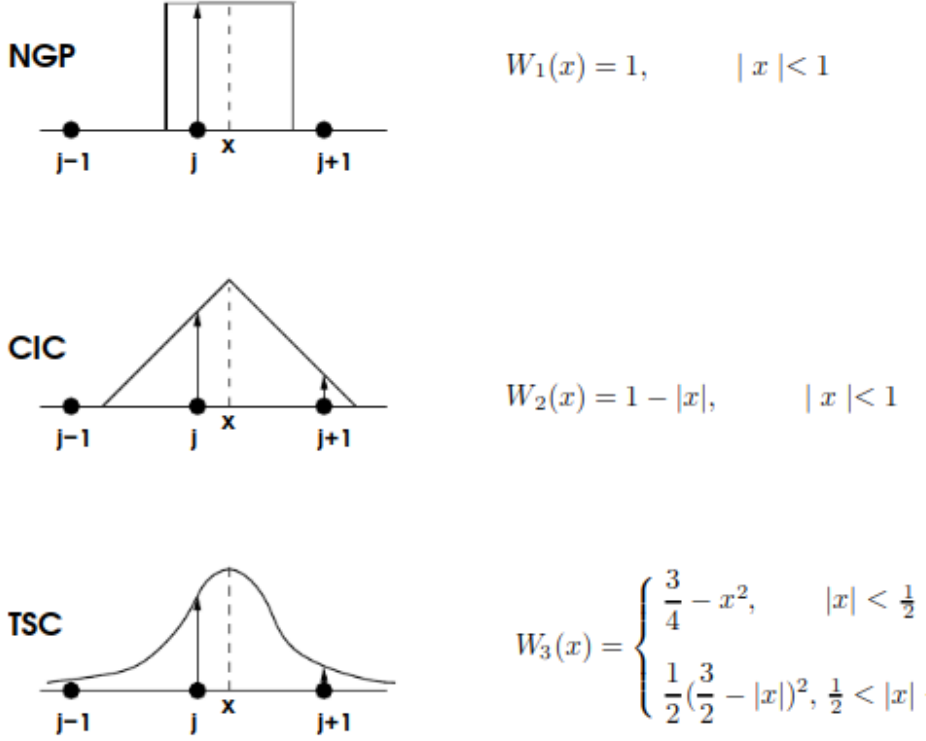


Figure 2.3: Density weighting schemes (Gibbon and Sutmann, 2002): a) NGP, b) CIC and c) TSC.

$$q_{i,j} = \frac{q_p}{A_{i,j}^2} (x_{i+1} - x)(y_{j+1} - y) \quad (2.1a)$$

$$q_{i+1,j} = \frac{q_p}{A_{i+1,j}^2} (x - x_i)(y_{j+1} - y) \quad (2.1b)$$

$$q_{i,j+1} = \frac{q_p}{A_{i,j+1}^2} (x_{i+1} - x)(y_{j+1} - y) \quad (2.1c)$$

$$q_{i+1,j+1} = \frac{q_p}{A_{i+1,j+1}^2} (x - x_i)(y - y_j) \quad (2.1d)$$

where,  $q_{i,j}$  is weighted charge of particle interpolated to the point  $(x_i, y_j)$ ,  $q_p$  is charge of particle located at  $(x, y)$  and  $A_{i,j} = \Delta x_i \Delta y_j$ .

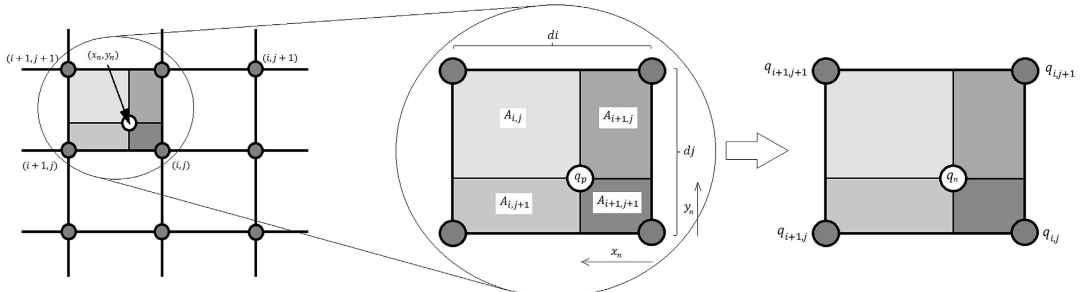


Figure 2.4: Schematic of Cloud-In-Cell algorithm. (Konior, 2017)

After all of the charges of the particles have been interpolated to their respective grid nodes, we will proceed to calculate the density across the grid. Since we now have the density over the grid, we are able to move on to the next step, which is integrating the field equation.

For electromagnetic PIC we use different Yee grid.

### 2.2.2 Integration of the Field Equations

As we discussed that for electrostatic Particle-in-Cell we solve Poisson's equation, which is given as (in 2-dimension):

$$\nabla^2 \phi = -\frac{\rho(x, y)}{\epsilon_0} \quad \text{or} \quad \frac{\partial^2 \phi}{\partial x^2} + \frac{\partial^2 \phi}{\partial y^2} = -\frac{\rho(x, y)}{\epsilon_0} \quad (2.2)$$

Once we get electric potential we can easily find electric field by solving following differential equation.

$$\mathbf{E} = -\nabla \phi \quad \text{or} \quad \mathbf{E}_x = -\frac{\partial \phi}{\partial x} \quad \text{and} \quad \mathbf{E}_y = -\frac{\partial \phi}{\partial y} \quad (2.3)$$

For fully fledged electromagnetic PIC we need to solve following sets of Maxwell's equations:

$$\frac{\partial \mathbf{E}}{\partial t} = \frac{1}{\mu_0 \epsilon_0} \nabla \times \mathbf{B} - \frac{1}{\epsilon_0} \mathbf{J} \quad (2.4a)$$

$$\frac{\partial \mathbf{B}}{\partial t} = -\nabla \times \mathbf{E} \quad (2.4b)$$

where equation: 2.4a is Maxwell-Ampère equation and equation: 2.4b is Maxwell-Faraday equation. Also magnetic field is solved on another type of spatial grid also known as Yee grid. In order for us to find a solution for these equations, we will need to discretize them over the grid point. There are a variety of mathematical approaches that can be used to solve them, and one of those approaches is the finite difference method combined with appropriate boundary conditions.

Let's now discuss about one of the techniques for numerically solving the Poisson equation in two dimensions. This uses a five-point stencil and the finite difference technique ([Genet Mekonnen Assefa, 2019](#)).

First of all we will have to discretize the Poisson equation over the spatial grid created in first step as follow:

$$\left( \frac{\partial^2 \phi}{\partial x^2} \right)_{x_i, y_j} = \frac{\phi_{i+1,j} + \phi_{i-1,j} - 2\phi_{i,j}}{\Delta x^2} + O(\Delta x^2) \quad (2.5a)$$

$$\left( \frac{\partial^2 \phi}{\partial y^2} \right)_{x_i, y_j} = \frac{\phi_{i,j+1} + \phi_{i,j-1} - 2\phi_{i,j}}{\Delta y^2} + O(\Delta y^2) \quad (2.5b)$$

For convenience we may choose  $\Delta x = \Delta y = h$ , otherwise solution will become more complicated and so Poisson's equation reduces to:

$$-\frac{\phi_{i+1,j} + \phi_{i-1,j} + \phi_{i,j+1} + \phi_{i,j-1} - 4\phi_{i,j}}{h^2} = f_{i,j}, \quad (2.6)$$

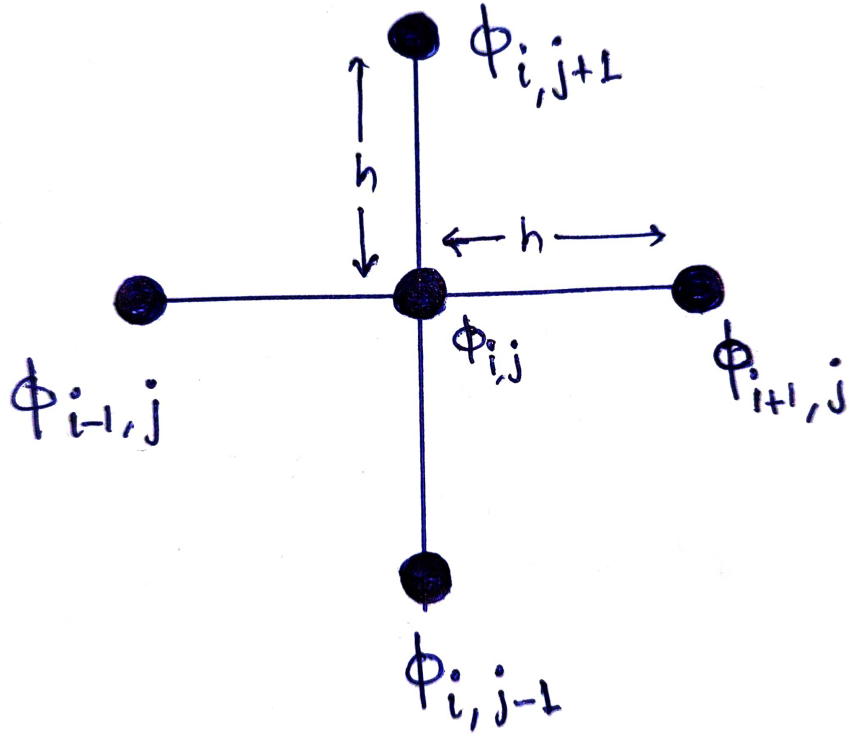


Figure 2.5: Five-Point-Stencil for Finite difference solver.

where  $f_{i,j}$  is charge density at point  $(x_i, y_j)$ . This is an elliptic equation (Hoffman, 2001) so we can solve it using the equation  $A\phi = F$ , where  $A$  and  $F$  is given as:

$$A = h^{-2} \begin{pmatrix} B & -I & & & \\ -I & B & -I & & \\ & \ddots & \ddots & \ddots & \\ & & -I & B & -I \\ & & & -I & B \end{pmatrix}, \quad \text{and} \quad (2.7)$$

$$B = \begin{pmatrix} 4 & -1 & & & \\ -1 & 4 & -1 & & \\ & \ddots & \ddots & \ddots & \\ & & -1 & 4 & -1 \\ & & & -1 & 4 \end{pmatrix} \quad (2.8)$$

Solving this matrix we will get the values of electric potential ( $\phi$ ) at each point, given that we know the boundary value. Now we have the electric potential we can find the electric field at each grid face by taking the negative gradient of electric potential as given by the equation 2.3. Now we can move to next step in PIC cycle.

### 2.2.3 Force/Field Weighting

After integrating the field equation, we are able to obtain the field; however, these fields are on the grid faces and are not present at the location where our particles are. We

will have to interpolate these field back to the particle's position. Most common method to accomplish this task is Inverse-Cloud-In-Cell (Inverse CIC). This task is very much similar to previous interpolation method. Now we have value and direction of field on particle's position so we are ready to move to next step of cycle.

### 2.2.4 Particle Push

Once we have the field at the particle we can use Lorentz's equation 2.9 to move particle and update it's position and velocity.

$$\frac{d\mathbf{v}}{dt} = \frac{q}{m}(\mathbf{E} + \mathbf{v} \times \mathbf{B}) \quad (2.9)$$

For this method we should use a scheme which have some kind of conservation. For electrostatic Particle-In-Cell Leapfrog ([Ahedo et al., 2007](#)) method is go to choice. Leapfrog integrator has following three component ([Birdsall and Langdon, 1991](#))

- Kick: particle's velocity is updated by half time step,  $\mathbf{v}_{i+1/2} = \mathbf{v}_i + \frac{\Delta t}{2}\mathbf{a}_i$
- Drift: particle's position is updated with  $\mathbf{v}_{i+1/2}$  velocity,  $\mathbf{r}_{i+1} = \mathbf{r}_i + \mathbf{v}_{i+1/2}\Delta t$
- Kick: again particle is kicked by half time step,  $\mathbf{v}_{i+1} = \mathbf{v}_{i+1/2} + \frac{\Delta t}{2}\mathbf{a}_i$

but this method fails when we try to include magnetic field. For the case of electromagnetic Particle-In-Cell a better scheme is there, known as Boris-Push scheme ([Birdsall and Langdon, 1991](#))([Boris, 1970](#)).

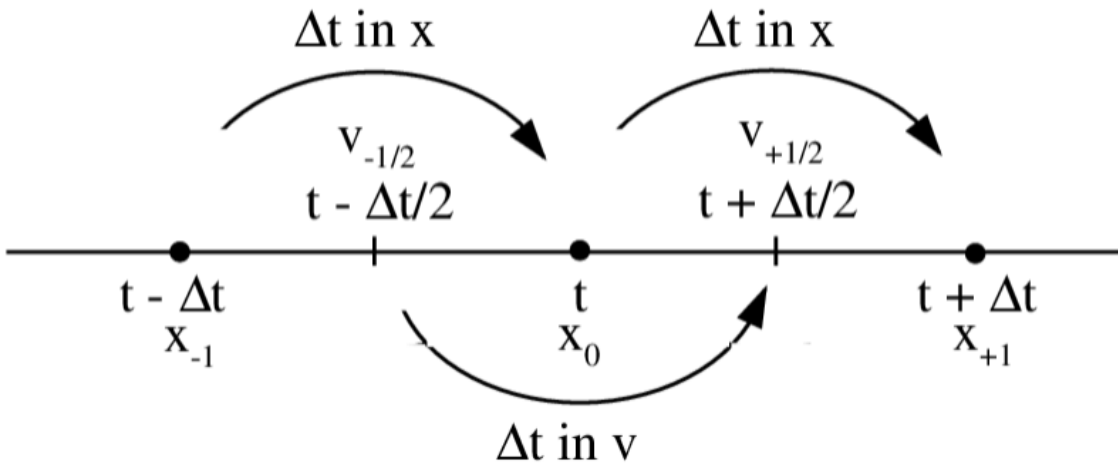


Figure 2.6: Schematic of Leapfrog integrator, it shows kick (first upward arrow), drift (downward arrow) and again kick (second upward arrow). ([Ahedo et al., 2007](#))

### Implementation of Boris Method

Lorentz equation (Eq.2.9) can be discretized as:

$$\frac{\mathbf{v}^{n+1/2} - \mathbf{v}^{n-1/2}}{\Delta t} = \frac{q}{m} \left[ \mathbf{E} + \frac{\mathbf{v}^{n+1/2} + \mathbf{v}^{n-1/2}}{2} \times \mathbf{B} \right] \quad (2.10)$$

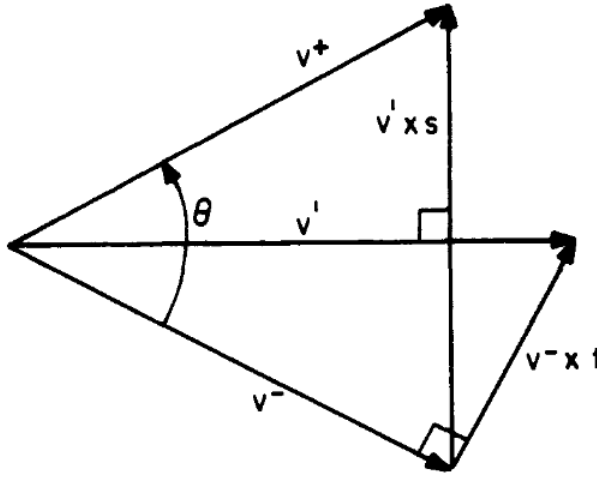


Figure 2.7: Velocity space depicting rotation from  $\mathbf{v}^-$  to  $\mathbf{v}^+$ . Projections of the total velocities onto the plane normal to the magnetic field are shown. [Birdsall and Langdon \(1991\)](#)

Now we have to eliminate the electric field term by introducing:

$$\mathbf{v}^{n-1/2} = \mathbf{v}^- - \frac{q\mathbf{E}}{m} \frac{\Delta t}{2} \quad (2.11a)$$

$$\mathbf{v}^{n+1/2} = \mathbf{v}^+ + \frac{q\mathbf{E}}{m} \frac{\Delta t}{2} \quad (2.11b)$$

Eq. 2.11 into Eq. 2.10 we will get pure rotation

$$\frac{\mathbf{v}^+ - \mathbf{v}^-}{\Delta t} = \frac{q}{2m} (\mathbf{v}^+ + \mathbf{v}^-) \times \mathbf{B} \quad (2.12)$$

now doing some basic geometry in Fig. 2.7 we can write  $\tan(\theta/2) = -(q\mathbf{a}_i B)m\Delta t/2$ . From here we can define  $\mathbf{t} = (q\mathbf{a}_i B/m)\Delta t/2$ .  $\mathbf{v}'$  (vector bisector) is given as:

$$\mathbf{v}' = \mathbf{v}^- + \mathbf{v}^- \times \mathbf{t} \quad (2.13)$$

as  $\mathbf{v}^+ - \mathbf{v}^-$  is parallel to  $\mathbf{v}' \times \mathbf{B}$  so we can write,

$$\mathbf{v}^+ = \mathbf{v}^- + \mathbf{v}' \times \mathbf{s} \quad (2.14)$$

where,

$$\mathbf{s} = \frac{2\mathbf{t}}{1 + \mathbf{t}^2} \quad (2.15)$$

Now that we have finally finished updating the position and velocity of our particles using an appropriate particle mover, our one cycle is complete. Now we should run the loop for N cycle where each cycle consist of all of the above mentioned steps.

# Chapter 3

## Getting hands on PIC: ePic (1D-Electrostatic PIC)

Theorizing is fine, but in order to acquire a more in-depth comprehension of physics behind kinetic simulation, we decided to write our very own two-dimensional electrostatic particle-in-Cell code. For our simulation, we implemented:

- Cloud-In-Cell (CIC) for charge weighting,
- Finite difference method to solver Poisson's equation,
- Inverse-CIC for field/force weighing and
- Leapfrog integrator and Boris-Pusher for particle mover

### 3.1 Interpolator Validation

Fig. 3.1 It is the result of our Cloud-In-Cell (CIC) based particle interpolator in PIC, which generates this output. Due to the fact that this is a two-dimensional particle mesh, the cloud-in-cell scheme will interpolate the weight of the particle across the four grid points that are closest to it. In this scenario, the node that has a greater number of neighbouring particles or that is located closest to the particles has a greater weight than the other nodes.

### 3.2 Field Solver validation

Fig. 3.2 is the plot that is produced as a result of solving two charged particles on the grid; one of the particles is positively charged (the red one), and another is negatively charged (the blue one), and both particles have the same magnitude of charge. It is the simplest case of an electric dipole. Field lines are generated by positively charged particles and annihilated by negatively charged particles. This is completely consistent with what we would anticipate from the electric fields produced by a dipole.

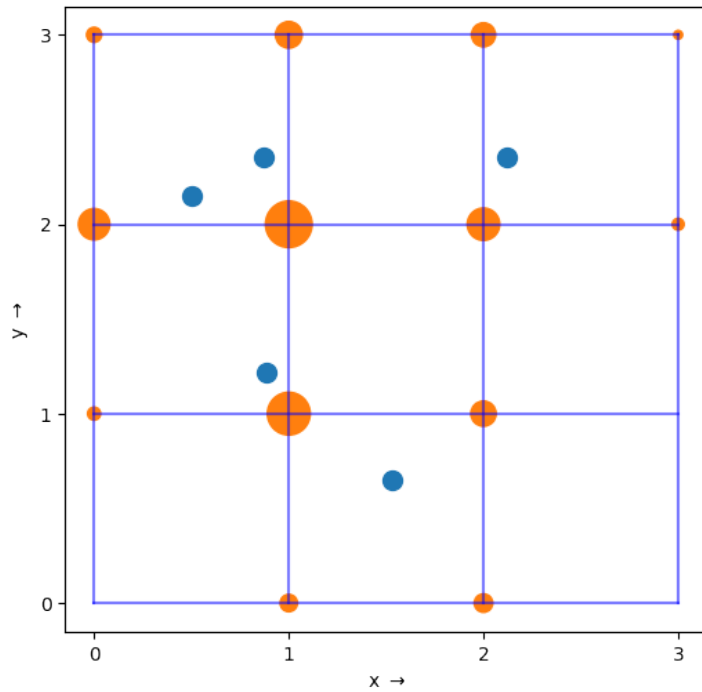


Figure 3.1: Particle Mesh generated by the script written by us with particle weighting using Cloud-in-Cell interpolation. Blue dots represent particles and orange dots represent their charges interpolated to grid points.

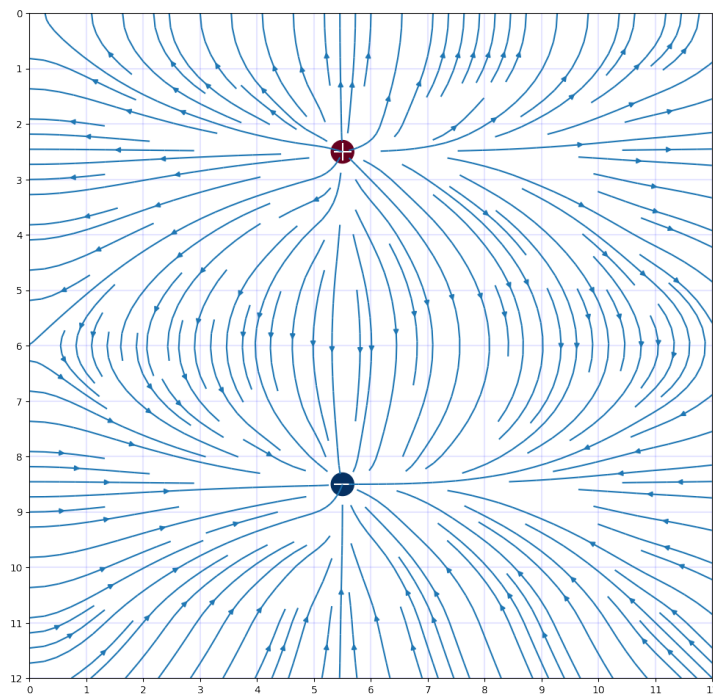


Figure 3.2: Electric field due to electric dipole obtained with field solver written by us. Red dot represents the positively charged particle and blue dot represent the negatively charged particle.

### 3.3 Particle Pusher Validation

We attempted to simulate the behavior of electrons when they were only allowed to move within a magnetic field. The plot of the same is shown in Fig. 3.3; it provides the trajectory according to what we would anticipate it to be.

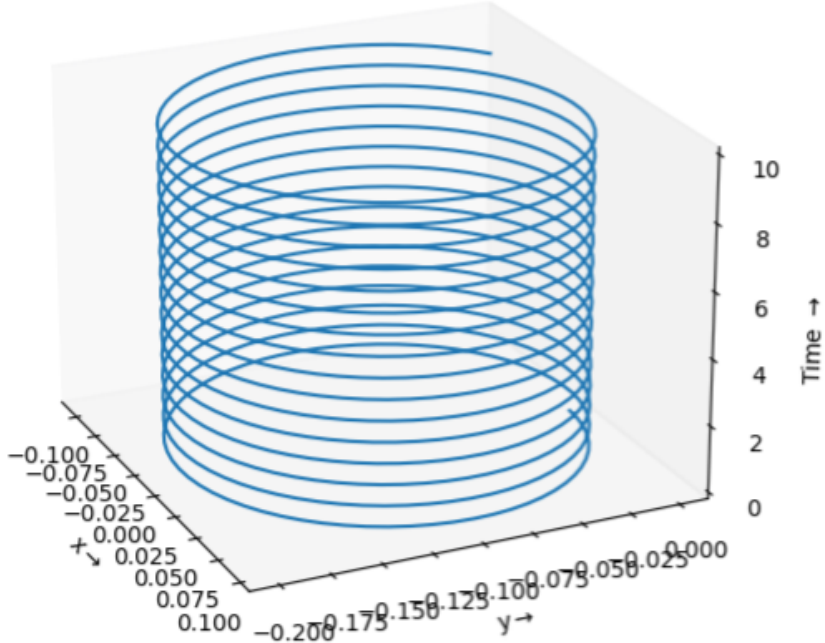
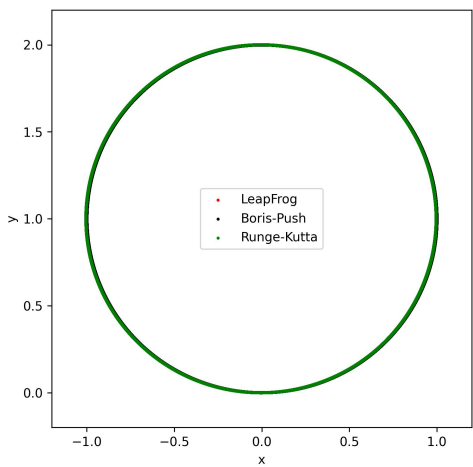


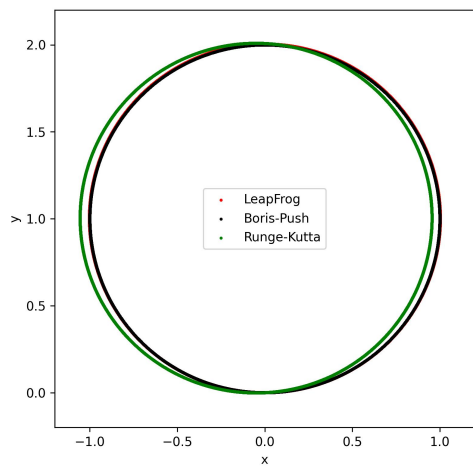
Figure 3.3: Path of electron in magnetic field using moved with Boris-Scheme.

We tried writing many different particle mover in Python with following parameters:  
 Electric field =  $(0, 0, 0)$   
 Magnetic field =  $(0, 0, 10)$   
 Mass of particle = 1  
 Charge on particle = 1  
 Initial Velocity =  $(-10, 0, 5)$   
 total time of simulation = 50  
 The result of the output is shown in the Fig. 2.7.

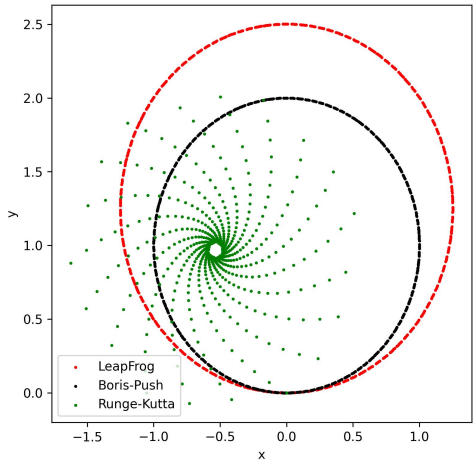
In this given setup the trajectory should be circle with radius of 1 unit centered at  $(0,1)$ . It can be clearly observe from the given Fig. 3.4, that Runge-Kutta ( $4^{th}$  order) started to diverge very soon and started going all over the place. After a certain time Leapfrog also started to diverge, but Boris Pusher keep giving correct result even the  $dt$  is as large as 2 in the given scenario. Despite being a non-symplectic(Qin et al., 2013) integrator Boris algorithm conserves phase space volume. The Boris algorithm is effective for the multi-scale dynamics of plasmas because it keeps the global bound on energy error that is typical of symplectic algorithms.



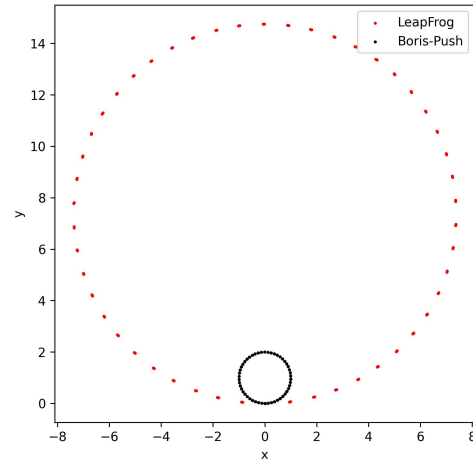
(a)  $dt = 0.001$



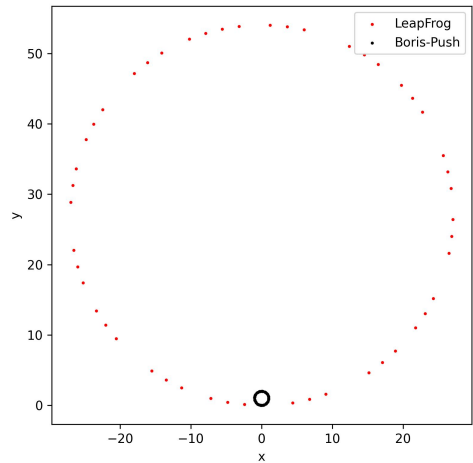
(b)  $dt = 0.01$



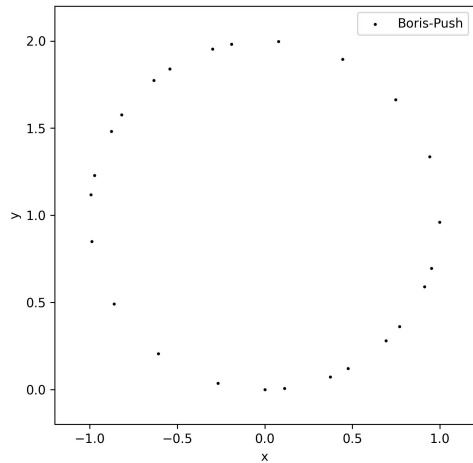
(c)  $dt = 0.1$



(d)  $dt = 0.5$



(e)  $dt = 1$



(f)  $dt = 2$

Figure 3.4: Out put of path of simulation of electron under magnetic field moved with three different integrator viz. Runge-Kutta, Leapfrog and Boris-Push.

## 3.4 Two Stream Instability test: A diagnostic for Electrostatic Particle-In-Cell

The two-stream instability is a well-known phenomenon in plasma physics, which occurs when two counter-propagating beams or populations of charged particles interact with each other. This interaction can lead to the growth of plasma waves and instabilities that can result in the exchange of energy between the particle populations and the waves ([Davidson \(1972\)](#); [Chen \(1984\)](#)).

The basic mechanism behind the two-stream instability can be understood as follows. When two streams of charged particles with different velocities move in opposite directions, they create an electrostatic field due to the charge separation between the populations. By absorbing energy from the relative motion of the two streams, this electrostatic field can in turn propel plasma waves that increase in amplitude. A new equilibrium point for the system may eventually be reached as a result of the growth of these waves, which may also cause a redistribution of particle energies and velocities ([Davidson \(1972\)](#); [Chen \(1984\)](#)).

The two-stream instability has been extensively studied in a variety of settings, including laboratory plasmas, space plasmas, and astrophysical environments. It has been found to play a significant role in processes such as beam-plasma interactions, particle acceleration, and energy transfer in these systems ([Fried \(1959\)](#); [Papadopoulos \(1988\)](#); [Gary \(1993\)](#)).

In conclusion, the two-stream instability is a fundamental plasma process that arises from the interaction between counter-propagating beams or populations of charged particles. It can lead to the growth of plasma waves and instabilities, ultimately resulting in the redistribution of particle energies and velocities. This process has been observed and studied in a wide range of plasma environments, highlighting its importance in understanding various plasma phenomena.

In order to verify the correctness of the code that we had written, we put it through this very well-known diagnostic procedure. During this test, we simulated the evolution of two electron beams that were travelling in opposite directions but at the same speed. When a slight perturbation is introduced the system becomes unstable. The results of the same are displayed in the upcoming figures.

To comprehend the fundamental physics underlying the kinetic modelling, we used the straightforward electrostatic Particle-In-Cell method, the accuracy of which is amply validated in this chapter. We will have to make significant modifications to incorporate a magnetic field and make significant optimizations to get our PIC ready for the simulation of complex plasma systems, though, because it is too simple to simulate complex plasma systems. Therefore, we moved on to Smilei, an electromagnetic PIC code that is already fully functional and have been heavily optimised. We will examine how it functions and what we attempted to simulate with it in the following chapter.

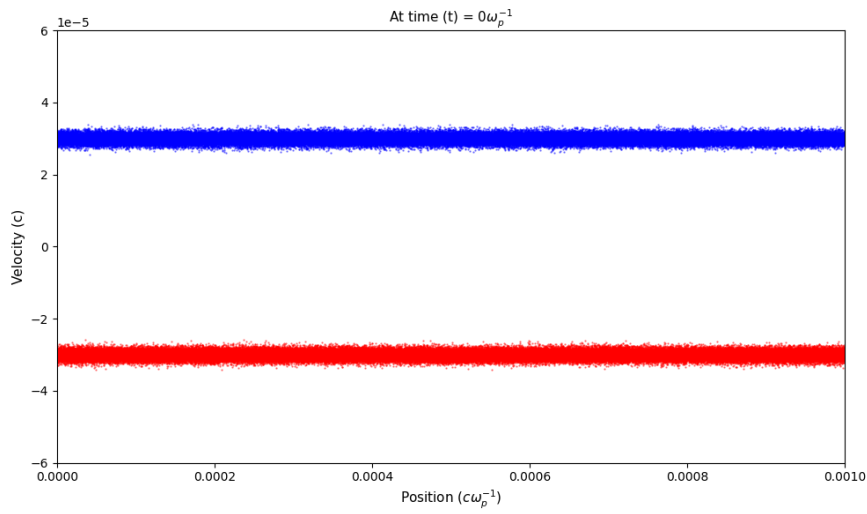


Figure 3.5: Two streams of electron flowing in opposite direction at initial time of simulation ( $t = 0\omega_p^{-1}$ ).

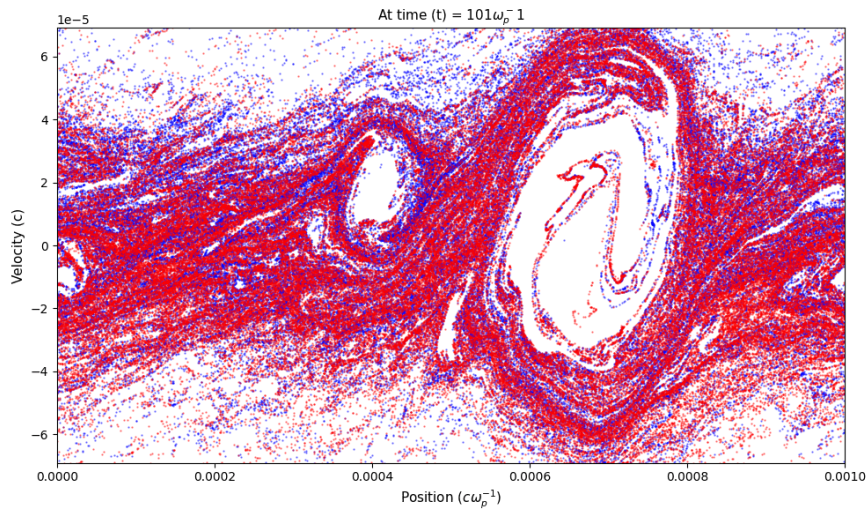


Figure 3.6: Two streams evolved into instability after  $t = 101\omega_p^{-1}$ . Here also red dots are particle initially moving in left direction and blue dots are moving in right direction at initial time.

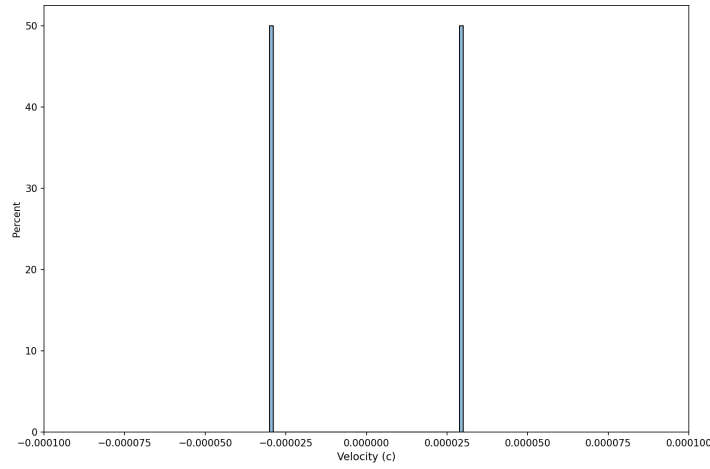


Figure 3.7: Velocity distribution of electron in two streams at initial state ( $t = 0\omega_p^{-1}$ ). Initially all particles are distributed into two part one with velocity of  $-3 \times 10^{-5}c$  and another  $3 \times 10^{-5}c$

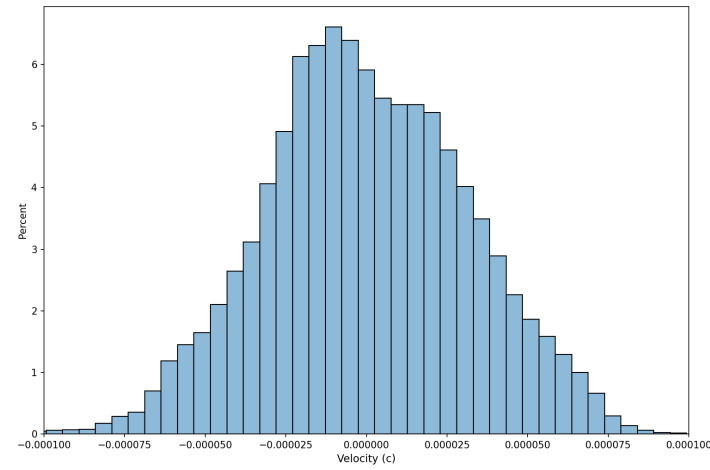


Figure 3.8: Velocity distribution after  $t = 101\omega_p^{-1}$ . The velocity is approaching zero. It should become gaussian with a mean of zero, but due to numerical error and our simulation's insufficient resolution, it is distributed as shown.

# Chapter 4

## Results: Plasmoid Instability in PIC

### 4.1 Smilei: Electromagnetic Particle-In-Cell

Smilei is a high-performance, massively parallel Particle-in-Cell (PIC) code, used for simulating plasmas in a variety of astrophysical and fusion applications. The code employs a hybrid Particle-in-Cell and Monte Carlo Collision (PIC-MCC) method, enabling it to efficiently simulate complex plasma phenomena. The code supports a wide range of physical models, including electromagnetic and electrostatic fields, plasma-neutral interactions, and ionization processes, among others ([Derouillat et al., 2018](#)).

Smilei implements various optimization strategies, including load balancing, parallel communication, and vectorization, to maximize the efficiency of the simulation. The code is written in C++ and parallelized using MPI (Message Passing Interface) and OpenMP (Open Multi-Processing) for distributed and shared memory parallelization, respectively ([Derouillat et al., 2018](#)).

In this work, we use Smilei to study magnetic reconnection in an asymmetric plasma. Smilei was chosen for its robustness and high performance, which allows for the efficient simulation of large-scale plasma systems. We employ the electromagnetic version of the code to accurately model the magnetic field dynamics during reconnection. Additionally, we use the code's ability to simulate multiple particle species, electron and proton in our case, to accurately capture the plasma dynamics during reconnection.

In chapter 2 we tried to give a brief idea about electrostatic PIC but here we will try to shed some light on electromagnetic PIC. Here we will try to give a brief description on how Smilei works.

#### 4.1.1 PIC algorithms in Smilei

Smilei works on Maxwell-Vlasov model which is described in brief in the section [1.3.3](#).

## superparticles

The Particle-In-Cell approach is so named because the distribution function  $f_s$  is discretized as the sum of N superparticles.

$$f_s(\mathbf{x}, t, \mathbf{p}) = \sum_{p=1}^{N_s} \frac{w_p}{V_c} S(\mathbf{x} - \mathbf{x}_p(t)) \delta(\mathbf{p} - \mathbf{p}_p(t)) \quad (4.1)$$

where  $w_p$  is the weight of a superparticles,  $\mathbf{x}_p$  and  $\mathbf{p}_p$  is its the position and momentum respectively,  $v_c$  is hypervolume of the cell,  $S$  represents shape function of all the superparticles and  $\delta$  is Dirac-delta distribution.

In Particle-In-Cell method, we integrate Vlasov Eq.1.17 along the trajectories of these superparticles, whereas Maxwell's Eq.1.18 are integrated over a discrete spatial mesh-grid, with cells referring to the spaces between consecutive grid points. Injecting Eq. 4.1 discrete distribution function into Vlasov Eq. 1.17, multiplying the result by P, and integrating over all P and the volume of the superparticles provides solutions to the relativistic equations of motion of isolated superparticles:

$$\frac{d\mathbf{x}_p}{dt} = \frac{\mathbf{u}_p}{\gamma_p} \quad (4.2)$$

$$\frac{d\mathbf{u}_p}{dt} = r_s \left( \mathbf{E}_p + \frac{\mathbf{u}_p}{\gamma_p} \times \mathbf{B}_p \right), \quad (4.3)$$

where  $r_s = q_s/m_s$  is charge to mass ratio for specy s.,  $y_p$  is the Lorentz factor and  $\mathbf{u}_p = \mathbf{p}_p/m_s$  is reduced momentum.

## Discretizing space and time

Smilei uses the Finite Difference Time Domain (FDTD) (Taflove et al., 2005) to solve Maxwell's equations. Yee gridis are use to discretize the electromagnetic fields in these methods, which facilitate for spatial-centering of the discretized curl operators in Maxwell's equations. The Fig.4.1 is a summary of how the electromagnetic fields, charge currents, and density currents are defined at different points along the Yee grid. Also, the time-centering of Maxwell's time-derivative is ensured by using integer time-steps ( $n$ ) for electric fields and half-integer time-steps ( $n + \frac{1}{2}$ ) for magnetic fields.

### 4.1.2 Computational cycle

Smilei is a particle-in-cell code that follows the same basic algorithm as other PIC codes. The code begins by initializing the simulation by loading all the quasiparticles and calculating the electromagnetic fields that are generated by these particles, as well as any external fields that are provided by the user. The code then enters the PIC loop, which executes for N time steps. Each iteration of the loop consists of four main steps:

1. interpolation of electromagnetic field at particle positions,
2. updating of the position and velocity of the particle,
3. projection of updated current and charge densities on the mesh-grid,
4. calculating updated electromagnetic field.

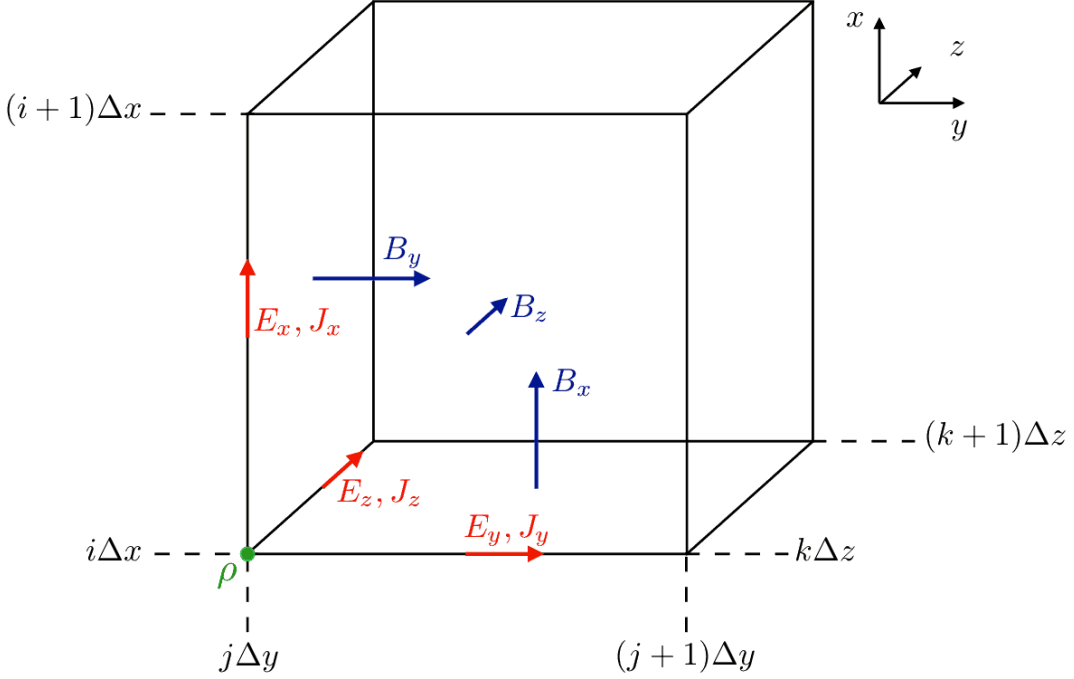


Figure 4.1: Yee lattice (Derouillat et al., 2018)

### Field Interpolation

Positions and velocities of the particles are known at the time-step ( $n$ ) and ( $n - \frac{1}{2}$ ) respectively at the starting of  $n^{th}$  timestep. Electromagnetic field at the position of particle  $p$ , at time step  $n$  is given as:

$$\mathbf{E}_p^n = V_c^{-1} \int d^3\mathbf{x} S(\mathbf{x} - \mathbf{x}_p^n) \mathbf{E}^n(\mathbf{x}), \quad (4.4a)$$

$$\mathbf{B}_p^n = V_c^{-1} \int d^3\mathbf{x} S(\mathbf{x} - \mathbf{x}_p^n) \mathbf{B}^n(\mathbf{x}) \text{ and} \quad (4.4b)$$

$$\mathbf{B}^n = \frac{1}{2} [\mathbf{B}^{n+1/2} + \mathbf{B}^{n-1/2}] \quad (4.4c)$$

For particle push it uses Relativistic, non-relativistic Boris pusher and Leapfrog integrator. The brief idea of some of which is already given in the section 2.2.4. Also brief introduction of interpolation methods are already given in the section 2.2.1.

### 4.1.3 PIC units

The vast majority of the PIC code deals only with variables and quantities that have no dimensions and so is the case for Smilei too. Before providing it as an input to the code, these variables and quantities need to have their values normalized. To normalize the results of all the other variables, one needs to select an appropriate reference variable. In the PIC code, the standard unit of measurement for speed is the speed of light, while charge and mass are specified in terms of the charge and mass of an electron. Also we define one of the most important quantity  $\omega_r$  as reference frequency, it represent

different different quantity based on the type of simulation. Once we have these necessary quantities we are not good to define other reference quantities here is the list

- reference time  $T_r = \frac{2\pi}{\omega_r}$
- reference length  $L_r = T_r c$
- reference temperature  $Temp_r = m_e c^2$
- reference energy  $K_r = m_e c^2$
- reference momentum  $P_r = m_e c$
- reference electric field  $E_r = m_e c \omega_r / e$
- reference magnetic field  $B_r = m_e \omega_r / e$
- reference particle density  $N_r = \epsilon_0 m_e \omega_r^2 / e^2$
- reference current density  $J_r = ce N_r$

Upon obtaining the reference quantity, the conversion of the physical unit to the code unit can be achieved by dividing it by the reference quantity of the corresponding quantity. To convert a physical unit of length into a code unit of length, the following steps must be taken:

$$L(\text{code unit}) = L(\text{physical unit}) / L_r$$

## 4.2 Our Setup for the simulation

To study the asymmetric magnetic reconnection in plasma we tried to simulate 5 different system. For our purpose we simulated the plasma condition on the boundary of magnetosphere and magnetosheath. For one of the simulation we used the data from the Magnetospheric Multiscale (MMS) mission ([Burch et al., 2016](#)).

### 4.2.1 Parameters used in input file

The simulation employs a two-dimensional, three-vector (2D3V) approach. Electromagnetic field boundaries are periodic in the x-direction, while Silver-Muller boundaries are applied in the y-direction. Particle boundaries are periodic in the x-direction and reflective in the y-direction. The magnetospheric magnetic field is set to 39.0 nT, while the magnetosheath magnetic field varies in each simulation according to the degree of asymmetry using the relationship  $B_{sheath} = 39.0 \text{ nT}/(\text{deg. of asym.})$ . The particle density in the magnetosphere is fixed at  $0.699 \times 10^{-6} \text{ m}^{-3}$ , while the magnetosheath particle density changes for each simulation as  $n_{sheath} = 3.95 \text{ m}^{-3} \times 10^{-6} \times (\text{deg. of asym.})^2$ . Proton temperatures are set at 1800 K in the magnetosphere and 320 K in the magnetosheath, while electron temperatures are 300 K and 28 K, respectively.

The simulation domain measures 96 x 12 in reference length units, equivalent to 67.8 km. Spatial resolution is achieved with 32 grid cells per unit reference length, and a temporal resolution of 500 steps per unit reference time. The total simulation time is 650

units of reference time. We employed a second-order interpolation method and the Boris relativistic particle pusher for particle motion. Each grid cell contains 32 protons and 32 electrons. The initial magnetic field is only provided in the x-direction, with no other external fields present. A Sigmoid function is used as a perturbation for the magnetic field in the x & y-direction. Field data and energy data were saved every 5000 time steps.

#### 4.2.2 Asymmetric Configurations: Magnetic Field and Density

In this study, we investigate the effects of asymmetry on magnetic reconnection by simulating plasma conditions in Earth's magnetosphere, where solar wind particles interact with the magnetosphere. We consider the region where solar wind encounters the magnetosphere as the magnetosheath. We maintain constant magnetic field, particle density, and other parameters within the magnetosphere while varying the magnetic field and particle density values in the magnetosheath to create different degrees of asymmetry.

The degrees of asymmetry considered for this study are as  $K = [1, 1.5, 2, 2.5, 3]$ . For each degree of asymmetry, we calculate the magnetic field in the magnetosheath ( $B_{sheath}$ ) and the particle density ( $n_{sheath}$ ) using the following equations:

$$B_{sheath} = 39.0/K \text{ nT}$$

$$n_{sheath} = 3.95e6 \times K^2 \text{ m}^{-3},$$

here K is degree of asymmetry

Below is a table summarizing the magnetic field ( $B_{sheath}$ ) and particle density ( $n_{sheath}$ ) values for each degree of asymmetry:

Degree of Asymmetry (K)	$B_{sheath}$ (nT)	$n_{sheath}$ ( $\text{cm}^{-3}$ )
1	39.0	3.95
1.5	26.0	8.89
2	19.5	15.80
2.5	15.6	24.69
3	13.0	35.55

Table 4.1: Magnetic field and particle density values for different degrees of asymmetry in the magnetosheath.

By using these magnetic field and particle density values, we create asymmetric configurations for each simulation, allowing us to investigate the effects of different levels of asymmetry on magnetic reconnection and plasmoid instability. The subsequent sections of this study will discuss the outcomes of the simulations, offering valuable insights into the significance of asymmetry in these phenomena and their potential implications for the field of magnetospheric physics.

The maintenance of equilibrium in the system requires the fulfillment of the pressure balance condition that is present between the magnetosphere and the magnetosheath. The principle of equilibrium stipulates that a constant value must exist for the aggregate pressure, encompassing both the magnetic and thermal pressures on both sides. The subsequent is a mathematical notation that can be employed to depict this phenomenon:

$$P_{magnetic,sphere} + P_{thermal,sphere} = P_{magnetic,sheath} + P_{thermal,sheath} \quad (4.5)$$

$$\frac{B_{sphere}^2}{2\mu_0} + n_{sphere}k_B(T_{p,sphere} + T_{e,sphere}) = \frac{B_{sheath}^2}{2\mu_0} + n_{sheath}k_B(T_{p,sheath} + T_{e,sheath}) \quad (4.6)$$

where  $P_{magnetic}$  is magnetic pressure  $P_{thermal}$  is thermal pressure;  $B_{sphere}$  and  $B_{sheath}$  represent the magnetic field strength in the magnetosphere and magnetosheath, respectively;  $n_{sphere}$  and  $n_{sheath}$  denote the particle density in the magnetosphere and magnetosheath, respectively;  $T_{p,sphere}$  and  $T_{e,sphere}$  represent the proton and electron temperatures in the magnetosphere, respectively, and  $T_{p,sheath}$  and  $T_{e,sheath}$  denote the proton and electron temperatures in the magnetosheath, respectively.;  $k_B$  is the Boltzmann constant, and  $\mu_0$  is the vacuum permeability.

By satisfying this pressure balance condition for each simulation, we ensure that the equilibrium is maintained in the presence of different degrees of asymmetry. This allows us to accurately analyze the impact of asymmetry on magnetic reconnection and plasmoid instability within a consistent framework.

## 4.3 Plasmoid Instability and Reconnection

Plasmoids are coherent magnetic structures that can form within a current sheet during the magnetic reconnection process ([Zhu and Wesson, 1995](#)). They are characterized by closed magnetic field lines and are associated with the release of magnetic energy. Plasmoid instability arises when the reconnecting current sheet becomes susceptible to the tearing mode instability, leading to the formation of multiple plasmoids that can coalesce or eject from the current sheet ([Loureiro et al., 2007](#)).

Plasmoid instabilities can significantly affect the dynamics of magnetic reconnection by altering the reconnection rate, the energy conversion processes, and the particle acceleration mechanisms.

Plasmoid instabilities have been shown to enhance the reconnection rate by facilitating the transport of magnetic flux and breaking up the reconnecting current sheet ([Comisso et al., 2016](#)).

[Cassak and Shay \(2012\)](#) investigated the impact of asymmetric configurations on plasmoid instability and magnetic reconnection. They found that the plasmoid instability is still present in asymmetric reconnection, but the threshold for the instability onset is altered due to the asymmetry. They also demonstrated that the asymmetry can affect the plasmoid size and the instability's growth rate, which we also observed in our simulations that we have shown up ahead in the upcoming subsection.

### 4.3.1 Plasmoids formation in our simulated systems for different degree of asymmetry (K)

The current density plot in the z-direction has been presented in this subsection, along with its overlap with the magnetic field in the x-y plane. The visualization of the mag-

netic field is represented through the use of lines and arrows, while the current density is depicted through a color gradient. The plots have been presented for various degrees of asymmetries denoted by the ratio of  $K = B_{sphere}/B_{sheath}$ . The external magnetic field in the magnetosphere remains constant throughout all simulations. However, to introduce asymmetry into the system, the initial external magnetic field in the magnetosphere is being altered for values of K equal to 1.0, 1.5, 2.0, 2.5, and 3.0.

The formation of plasmoids is observable in the depicted plots. The reconnections initiate from the central region where a perturbation has been introduced, subsequently leading to the formation of numerous plasmoids. Over a period of time, the plasmoid undergoes coalescence, resulting in the formation of larger plasmoids. The X-points and magnetic reconnections are also observable. The plots demonstrate a clear convergence of magnetic fields and a subsequent alteration in their geometric configuration in reconnection region.

The plots indicate that the reconnection rate in the first system ( $K = 1$ ) is significantly greater than in the remaining systems. Furthermore, as the value of K increases, the reconnection rate in the system decreases. All of these simulations are run for same amount of time, but the rate of reconnection seems to decreasing as the value of K increases so we do not see that much dominant plasmoids in the systems with higher K as compared to  $K = 1$ .

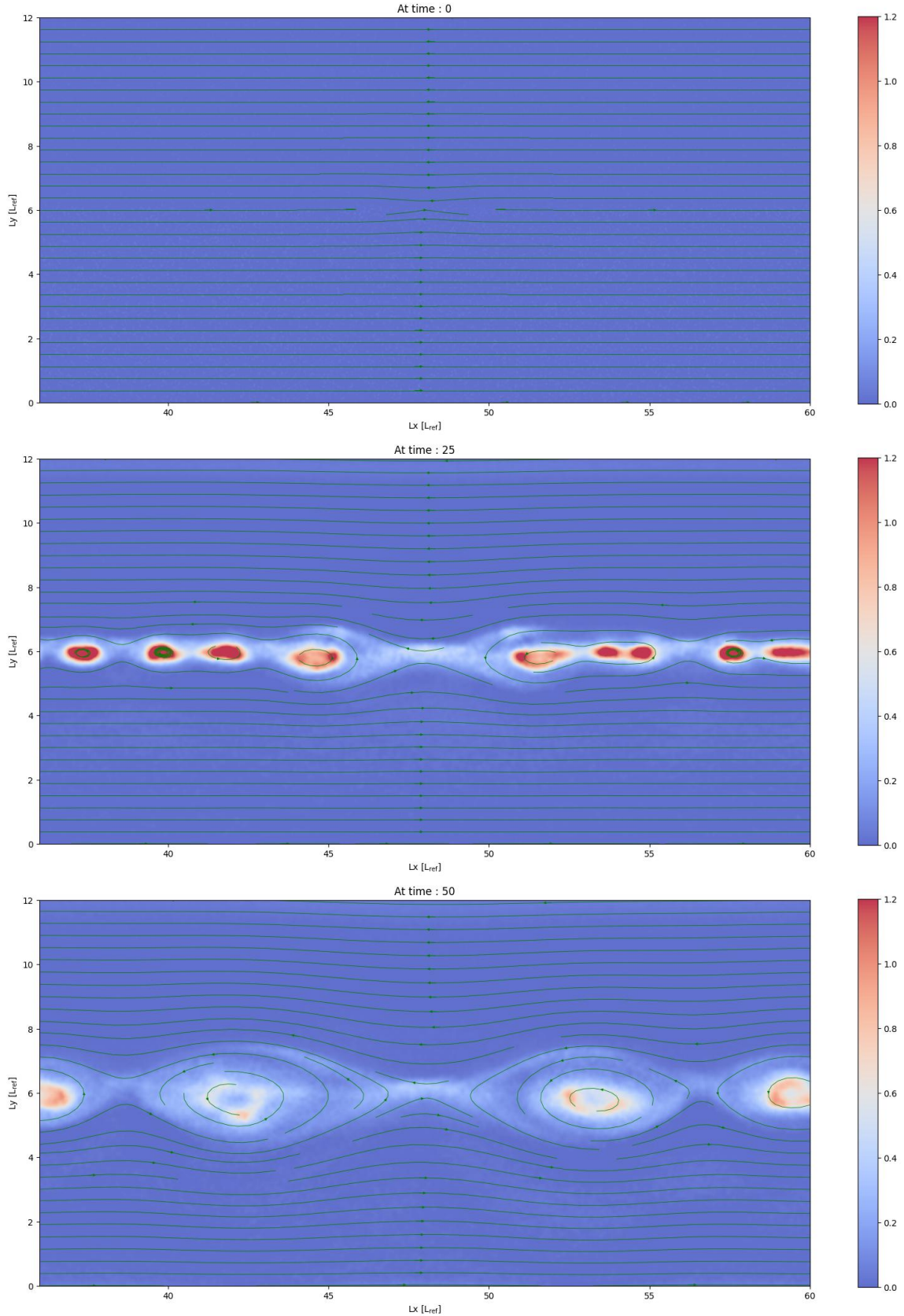


Figure 4.2: These images show the evolution of current density in  $z$ -direction for  $K = 1$ . The lines with arrow show the direction of magnetic field in  $x$ - $y$  plane. The image on the top is snapshot at  $t = 0\omega_p^{-1}$ , image on the middle is snapshot at  $t = 250\omega_p^{-1}$  and the bottom is at  $t = 500\omega_p^{-1}$ , here  $\omega_p$  is the plasma frequency.

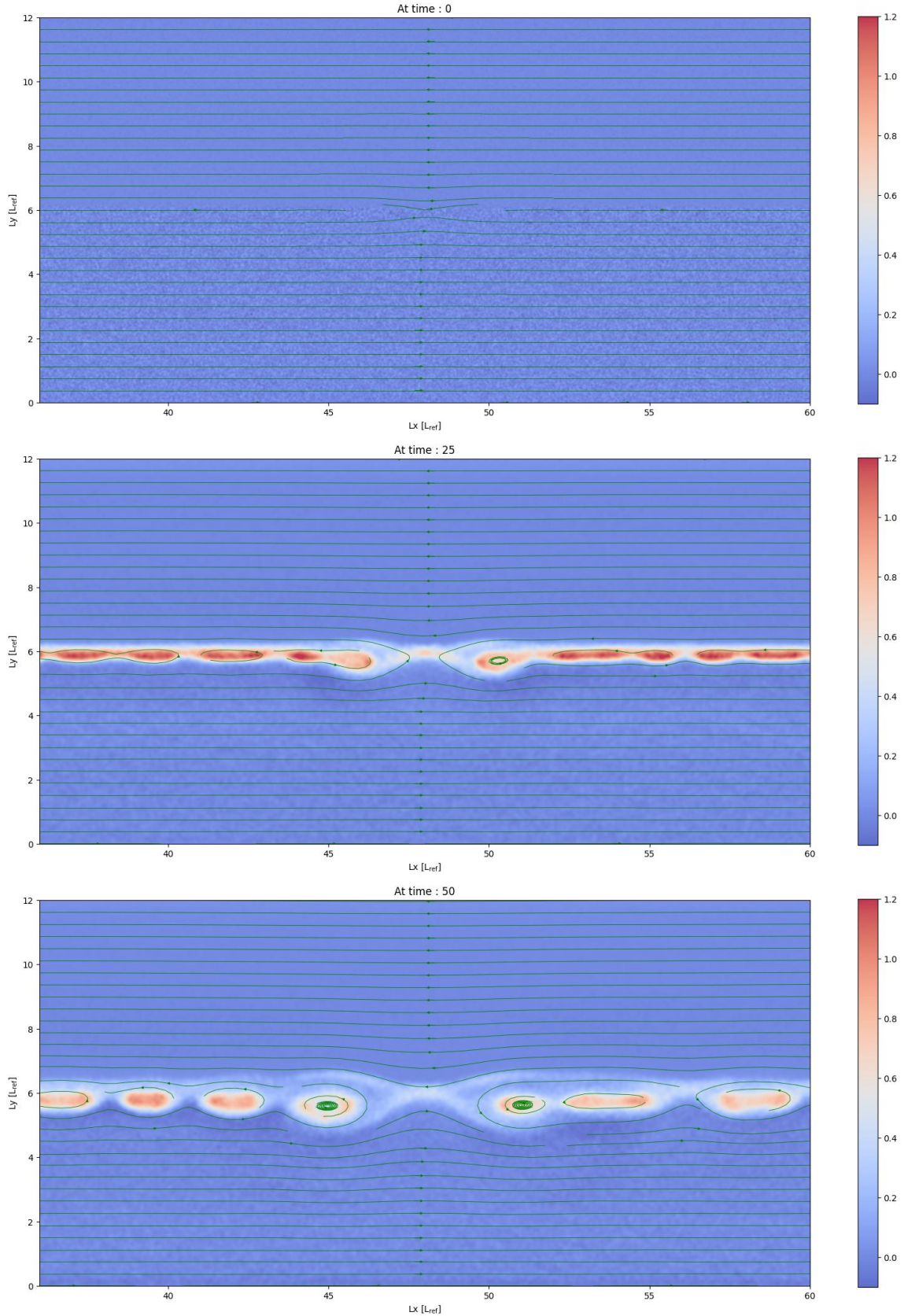


Figure 4.3: These images show the evolution of current density in z-direction for  $K = 1.5$ . The lines with arrow show the direction of magnetic field in x-y plane. The image on the top is snapshot at  $t = 0\omega_p^{-1}$ , image on the middle is snapshot at  $t = 250\omega_p^{-1}$  and the bottom is at  $t = 500\omega_p^{-1}$ , here  $\omega_p$  is the plasma frequency.

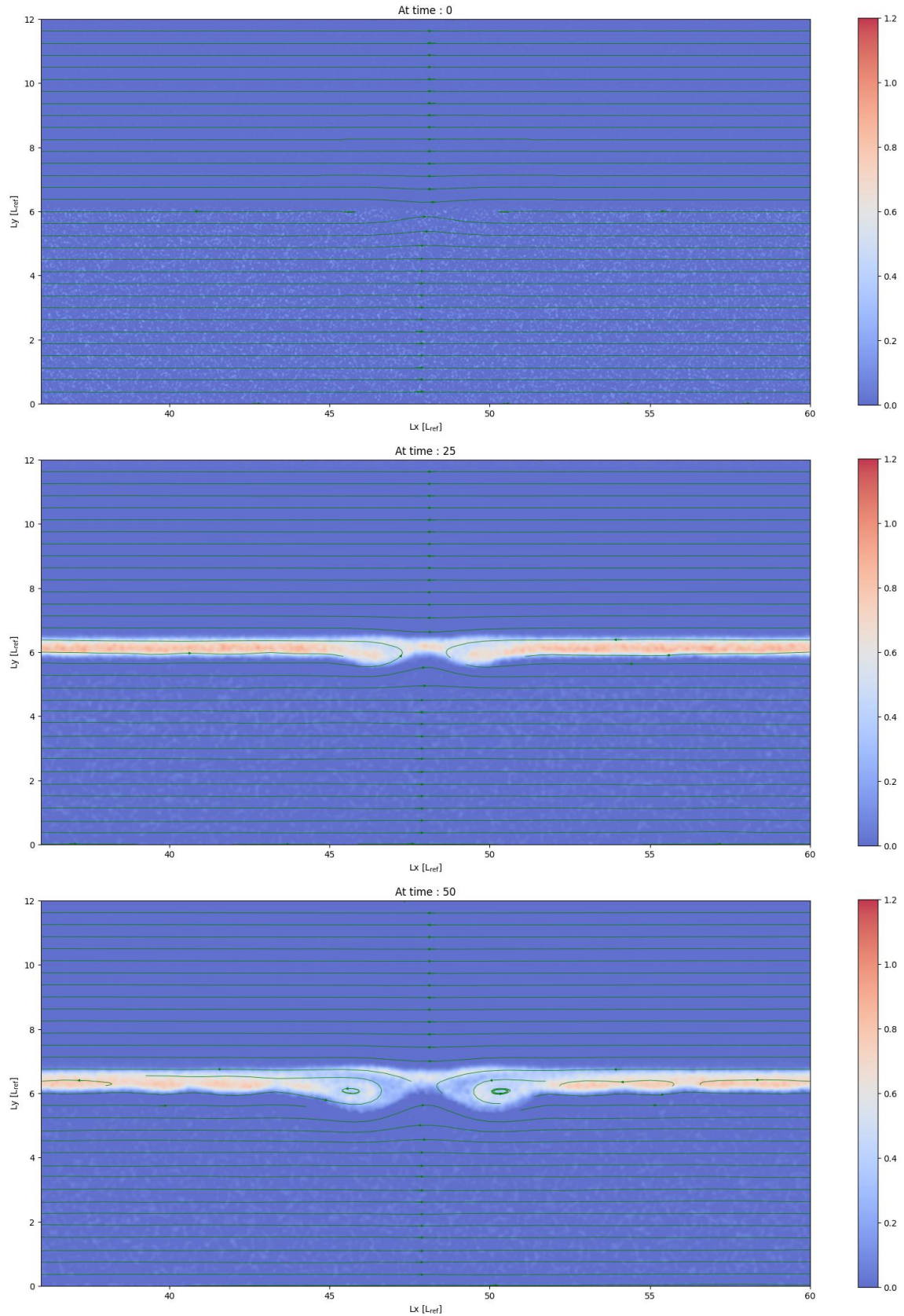


Figure 4.4: These images show the evolution of current density in z-direction for  $K = 2$ . The lines with arrow show the direction of magnetic field in x-y plane. The image on the top is snapshot at  $t = 0\omega_p^{-1}$ , image on the middle is snapshot at  $t = 250\omega_p^{-1}$  and the bottom is at  $t = 500\omega_p^{-1}$ , here  $\omega_p$  is the plasma frequency.

## 4.4 Reconnection Rate

The magnetic reconnection rate quantifies the speed at which magnetic field lines break and reconnect, playing a crucial role in the conversion of magnetic energy into kinetic and thermal energy. The reconnection rate is often represented by a dimensionless parameter, typically denoted as the "reconnection rate coefficient". Several factors influence the reconnection rate, including plasma resistivity, magnetic field configuration, and the presence of instabilities such as the plasmoid instability ([Priest and Forbes, 2000b](#)).

Recent studies have shown that the plasmoid instability can further increase the reconnection rate by breaking up the current sheet and facilitating magnetic flux transport ([Daughton et al., 2011](#)).

Experimental and numerical studies have confirmed the occurrence of fast magnetic reconnection in various plasma environments, with reconnection rates much higher than those predicted by the Sweet-Parker model ([Yamada et al., 1999](#)). This enhancement in the reconnection rate has significant implications for energy release and particle acceleration in astrophysical and laboratory plasmas.

The calculation of the reconnection rate involves determining the summation of the mean values of the electric field magnitude, specifically  $E_z$ , within two narrow strips ( $\Delta y = 1.0 L_r$ ) that are situated along the two current sheets and subsequently normalizing it with  $B_0 v_A$ . The mathematical representation for the aforementioned is as follows ([Paul, 2020](#)):

$$E_{\text{rec}} = \frac{1}{B_0 v_A} \left( \left| \left| \frac{\int_{-y_1}^{y_2} \int_{x_1}^{x_2} E_z dx dy}{\int_{-y_1}^{y_2} \int_{x_1}^{x_2} dx dy} \right| \right| + \left| \left| \frac{\int_{-y_2}^{-y_1} \int_{x_1}^{x_2} E_z dx dy}{\int_{-y_2}^{-y_1} \int_{x_1}^{x_2} dx dy} \right| \right| \right) \quad (4.7)$$

The volume average of  $E_z$  over the grid has been selected as the metric to gauge reconnection rate. This choice is motivated by the observation that in our system, the plasma undergoes motion in the  $y$ -direction within the reconnection region, while the reconnecting magnetic field is oriented in the  $x$ -direction. Consequently, when the magnetic field undergoes a change due to breaking and connecting, it induces an electric field in the  $z$ -direction, refer to Eq. 4.8. Hence, the electric field oriented along the  $z$ -axis provides an accurate representation of the rate of reconnection.

### 4.4.1 Reconnection rates of our five simulations

Utilizing a consistent methodology, the reconnection rates were computed for each of the five simulations exhibiting varying degrees of asymmetry. The graph depicting the aforementioned information is presented below. Based on the presented plots, it can be inferred that systems possessing lower  $K$  values exhibit a comparatively greater reconnection rate. One major factor causing producing this result must be lower magnitude of magnetic field in magnetosheath.

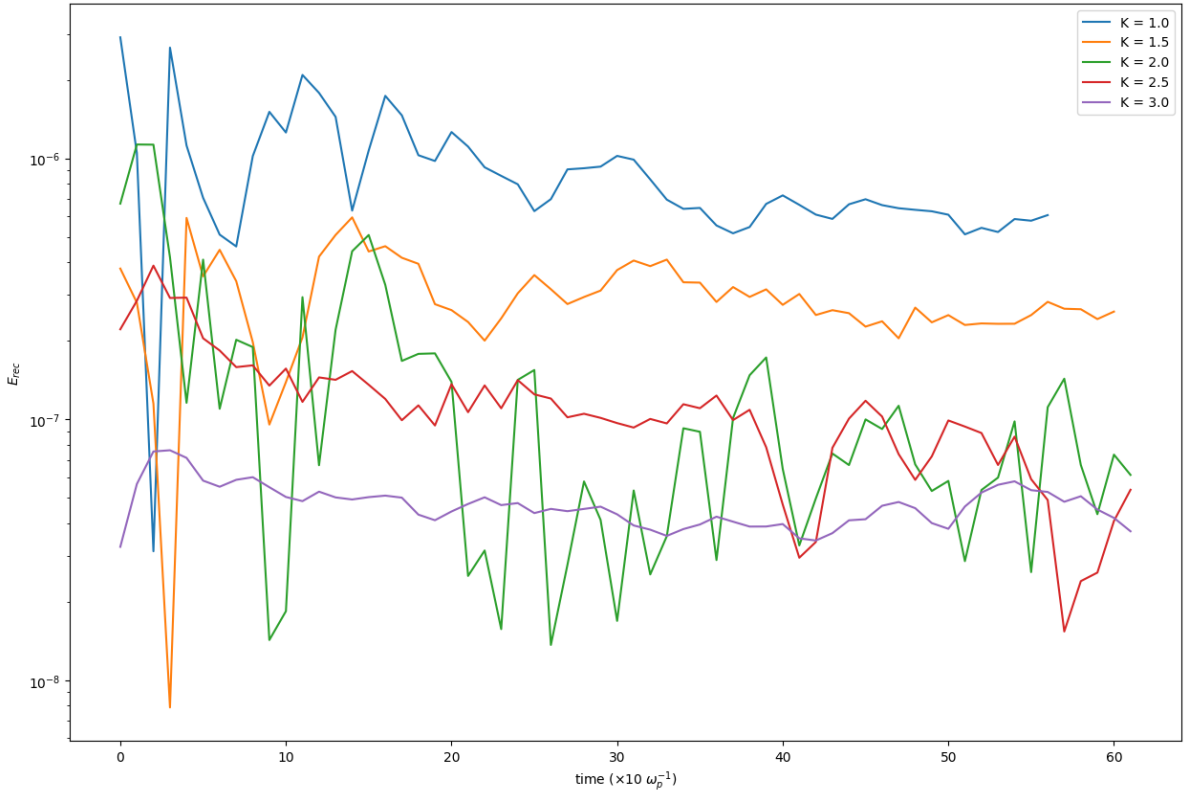


Figure 4.5: The plot illustrates the variation of reconnection rate over time for five distinct degrees of symmetry. The logarithmic scale is utilized for the y-axis to indicate the magnetic reconnection rate, whereas the x-axis denotes the time ( $\times 10 \omega_p^{-1}$ ), here  $\omega_p^{-1}$  is plasma frequency. Note that in this plot we have moving average with windows of 3 data points to smoothen the graph a bit.

#### 4.4.2 Average reconnection rates for different simulations

In order to conduct a more comprehensive analysis of the system, we generated a plot that depicts the average reconnection rate as a function of the degree of asymmetry. This approach enables us to gain insight into the relationship between changes in asymmetry and corresponding changes in the reconnection rate. Below we have presented the table of the same:

Degree of Asymmetry (K)	$B_{sheath}$ (nT)	$n_{sheath}$ (cm $^{-3}$ )	$E_{rec,avg} (\times 10^{-6})$	$E_{rec,max} (\times 10^{-6})$
1.0	39.0	3.95	1.06	7.73
1.5	26.0	8.89	3.58	1.97
2.0	19.5	15.80	0.16	1.28
2.5	15.6	24.69	0.16	0.76
3.0	13.0	35.55	0.05	0.09

Table 4.2: The tabular data presented herein depicts the average and maximum reconnection rates across varying degrees of system asymmetry.

After obtaining the data-set containing the average rate values for varying degrees of asymmetry, we attempted to model the resulting curves using the equation:

$$E_{rec,avg} = Ae^{-\alpha K}$$

and we got the value of  $A = 3.606 \times 10^{-6}$  and  $\alpha = 1.406$ . Our study's aim was to find a relationship between the rate and the asymmetry of the system. We noticed that as asymmetry increases, the system's average rate of reconnection is found to be decreasing over time.

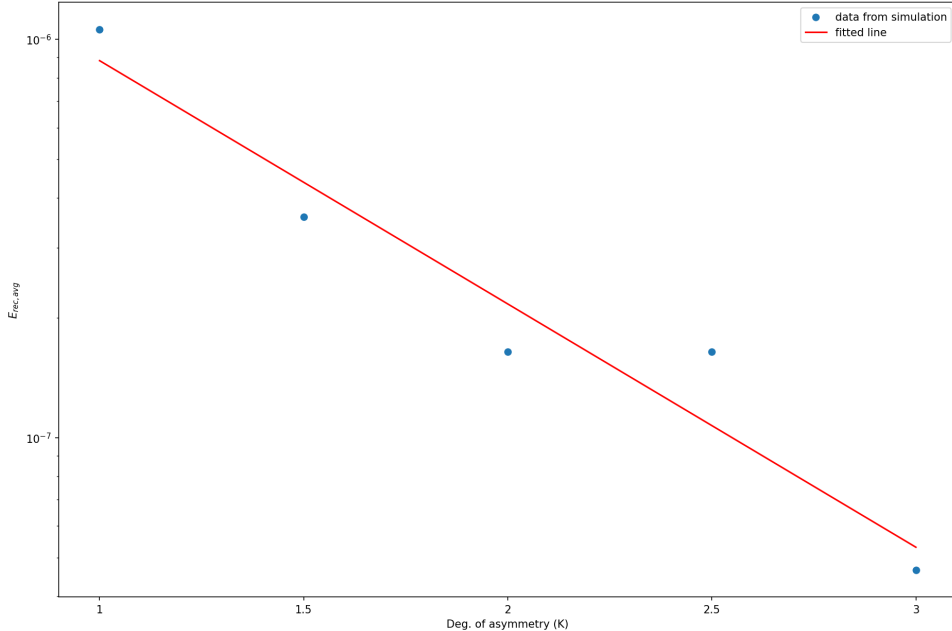


Figure 4.6: Plot of the average reconnection rate ( $E_{rec,avg}$ ) with varying degrees of asymmetry (K), Dots represent the data we obtained from the simulations, and the line represents the curve fitted with the equation  $E_{rec,avg} = Ae^{-\alpha K}$ .

### Chi-Square Test for goodness of fit:

The chi-square test was utilized to assess the goodness of fit. Following is the quick review of how to perform chi-square test for goodness of fit.

1. Obtain the observed and expected data: Determine the observed y-values ( $y_{obs}$ ) and calculate the expected y-values ( $y_{fit}$ ) model used for fitting.
2. Compute the residuals: Calculate the difference between the observed y-values ( $y_{obs}$ ) and expected y-values ( $y_{fit}$ ) for each data point.
3. Calculate the chi-square value ( $\chi^2$ ): Compute the chi-square value using the formula:  $\chi^2 = \sum_{i=1}^n \frac{(y_{obs,i} - y_{fit,i})^2}{y_{fit,i}}$ .
4. Determine the degrees of freedom (df): Calculate the degrees of freedom as  $df = n - p$ , where  $n$  is the number of data points and  $p$  is the number of fit parameters (2 for a linear fit with slope and intercept).
5. Compute the p-value: Calculate the p-value using the chi-square cumulative distribution function (CDF) with the calculated  $\chi^2$  and  $df$  values.
6. Interpret the p-value: Compare the p-value with your chosen significance level (e.g., 0.05 for a 95% confidence level) to determine if the linear fit is a good representation of the data.

Below table represent the result of chi-square test:

Table 4.3: Chi-square test result

	Average Rate
Model	$E_{rec,avg} = Ae^{-\alpha K}$
A	$3.606 \times 10^{-6}$
$\alpha$	1.406
$\chi^2$	$9.27 \times 10^{-8}$
Degree of Freedom	3
P-value	$\approx 1$

## 4.5 Energy bifurcation during magnetic reconnection

During magnetic reconnection, energy bifurcation plays a crucial role in the redistribution of magnetic, kinetic, and thermal energies within the plasma. This process involves the conversion of magnetic energy into kinetic and thermal energies, ultimately affecting the overall dynamics of the system. Magnetic reconnection causes a rapid release of magnetic energy, leading to the acceleration of charged particles in the plasma. This accelerated motion of particles results in the conversion of magnetic energy into kinetic energy, subsequently increasing the plasma's overall kinetic energy (Hesse et al., 2014).

Furthermore, the heating of plasma during magnetic reconnection is another important aspect of energy bifurcation. The increased kinetic energy of the plasma particles eventually gets transferred to thermal energy through particle collisions, resulting in a rise in plasma temperature ([Hesse et al., 2014](#)). The energy bifurcation phenomenon during magnetic reconnection has significant implications for various space and astrophysical phenomena, such as solar flares and magnetic substorms in Earth's magnetosphere, where rapid energy conversion and redistribution are observed [Birn and Hesse \(2005\)](#).

The temporal evolution of scalar data was derived from the output file. The data encompassed total energy, magnetic field energy, electric field energy, and kinetic energy. In the subsequent sections, we will conduct a detailed analysis of each of them individually.

#### 4.5.1 Magnetic field energy

As we know that in the system with magnetic reconnection, opposite the magnetic field lines come closer and snap to change the configuration which leads to conversion of magnetic field energy into other type of energy viz. electric field energy, kinetic energy or thermal energy. So in ideal scenario we expect that as system evolves the magnetic field energy should decrease.

In our simulations, we observe a significant decrease in magnetic energy for systems with  $K = 1$  and  $K = 1.5$ . However, the change is relatively small for the system with  $K = 2$ . This behavior aligns with our expectations for systems with higher  $K$  values, which exhibit lower reconnection rates, leading to reduced dissipation of magnetic energy. Moreover, as the asymmetry increases, the magnetic field on the other side of the system decreases, resulting in a lower total magnetic energy.

Intriguingly, for  $K = 2.5$  and  $K = 3$ , the kinetic energy increases for reasons that remain unclear. Further investigation is required to verify this observation, which may be attributable to the highly complex nature of the system when the asymmetry increases. It is possible that the equilibrium between the two sides of the system is disrupted in these cases. This disruption could be due to the propagation of plasmoids and current sheets towards the region with a lower magnetic field, which might impact the energy conversion processes occurring during magnetic reconnection. The observed increase in kinetic energy could also be associated with complex plasma dynamics, such as changes in the particle distribution function or interactions with other plasma structures.

To obtain a comprehensive understanding of this phenomenon, additional simulations and analyses will be necessary. A more in-depth exploration of the underlying physics, including the role of plasmoid instabilities, particle acceleration, and the influence of various plasma parameters, may shed light on the observed behavior and improve our understanding of the complex interplay between magnetic and kinetic energies in asymmetric magnetic reconnection processes.

For the system with  $K = 1, 1.5$  and  $2$ , in the total magnetic field energy of the system we observed an initial sharp decrease followed by a rise and then another decrease, could be attributed to the complex dynamics of the magnetic reconnection process and the interplay of different physical mechanisms. One possible explanations for the observed

behavior could be the formation of plasmoids and secondary magnetic islands: During the magnetic reconnection process, instabilities can develop in the current sheet, leading to the formation of plasmoids or secondary magnetic islands. These structures can temporarily store magnetic energy, causing an increase in the overall magnetic energy after the initial sharp decrease. As the reconnection process continues and the plasmoids merge or are ejected from the reconnection region, the magnetic energy starts to decrease again.

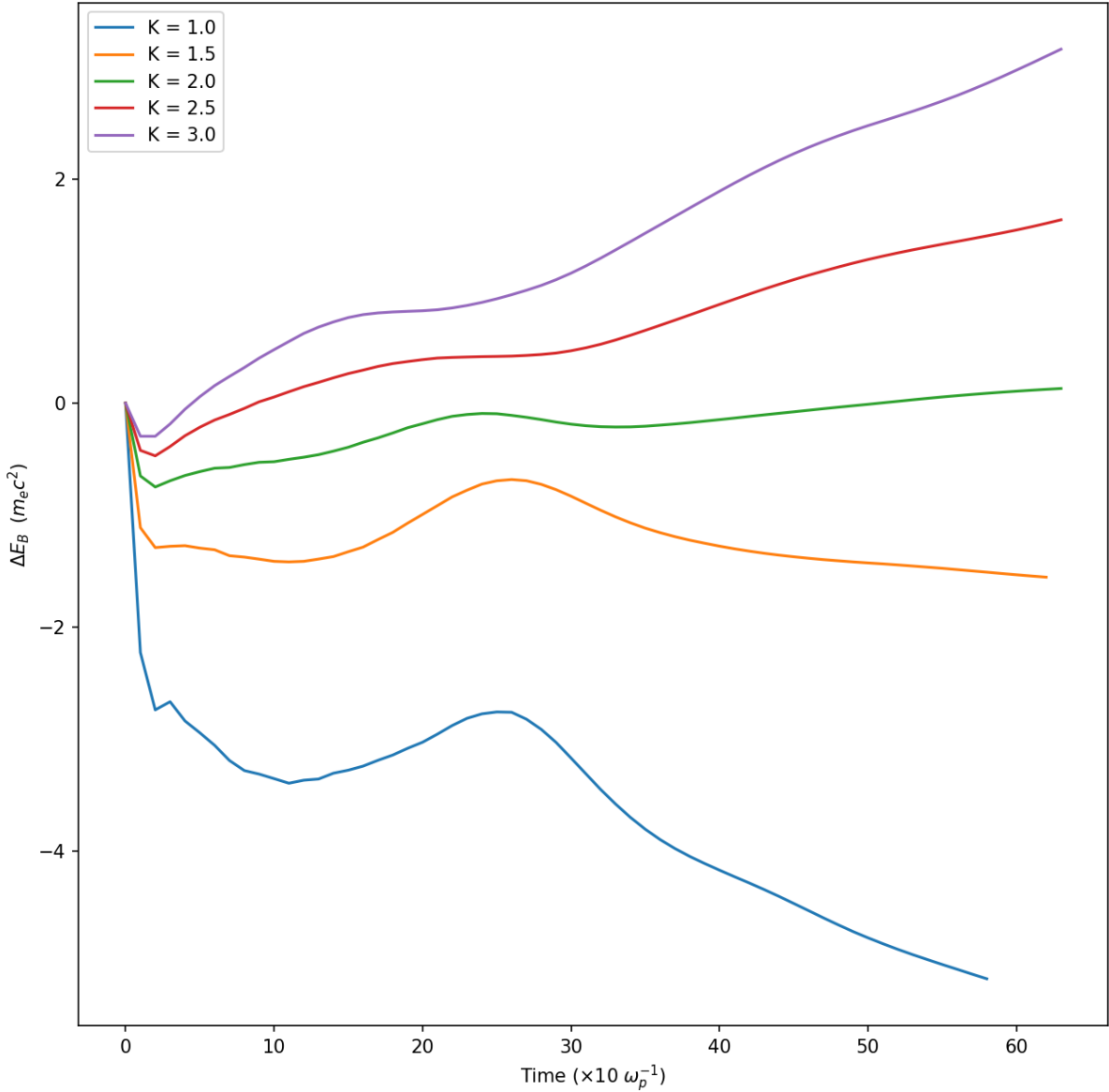


Figure 4.7: Plot of change in total magnetic field energy ( $\Delta E_B = E_{B,t} - E_{B,0}$ ) of the system with time ( $\times 10 \omega_p^{-1}$ ). We have illustrated here the trend for magnetic energy evolution with time for all five degree of asymmetries (K).

#### 4.5.2 Electric field energy

From the generalised Ohm's law we can see that, as magnetic field lines approach the reconnection region, the plasma velocity  $\mathbf{v}$  and the magnetic field ( $\mathbf{B}$ ) become perpendic-

ular, causing the  $\mathbf{v} \times \mathbf{B}$  term to be non-zero. This term represents the convective electric field induced by the motion of charged particles in the magnetic field.

$$\mathbf{E} + \mathbf{v} \times \mathbf{B} = \eta \mathbf{J} + \frac{\mathbf{J} \times \mathbf{B}}{en} + \frac{\nabla \cdot \tilde{P}_e}{en} + \frac{m_e}{e} \frac{d\mathbf{v}_e}{dt} \quad (4.8)$$

Also the breaking and reconnecting of magnetic field lines involve changes in the magnetic field configuration and a decrease in magnetic energy. According to Faraday's law of electromagnetic induction, a changing magnetic field generates an electric field. In the reconnection region, the rapid change in the magnetic field leads to the formation of a localized electric field.

$$\nabla \times \mathbf{E} = -\frac{\partial \mathbf{B}}{\partial t} \quad (4.9)$$

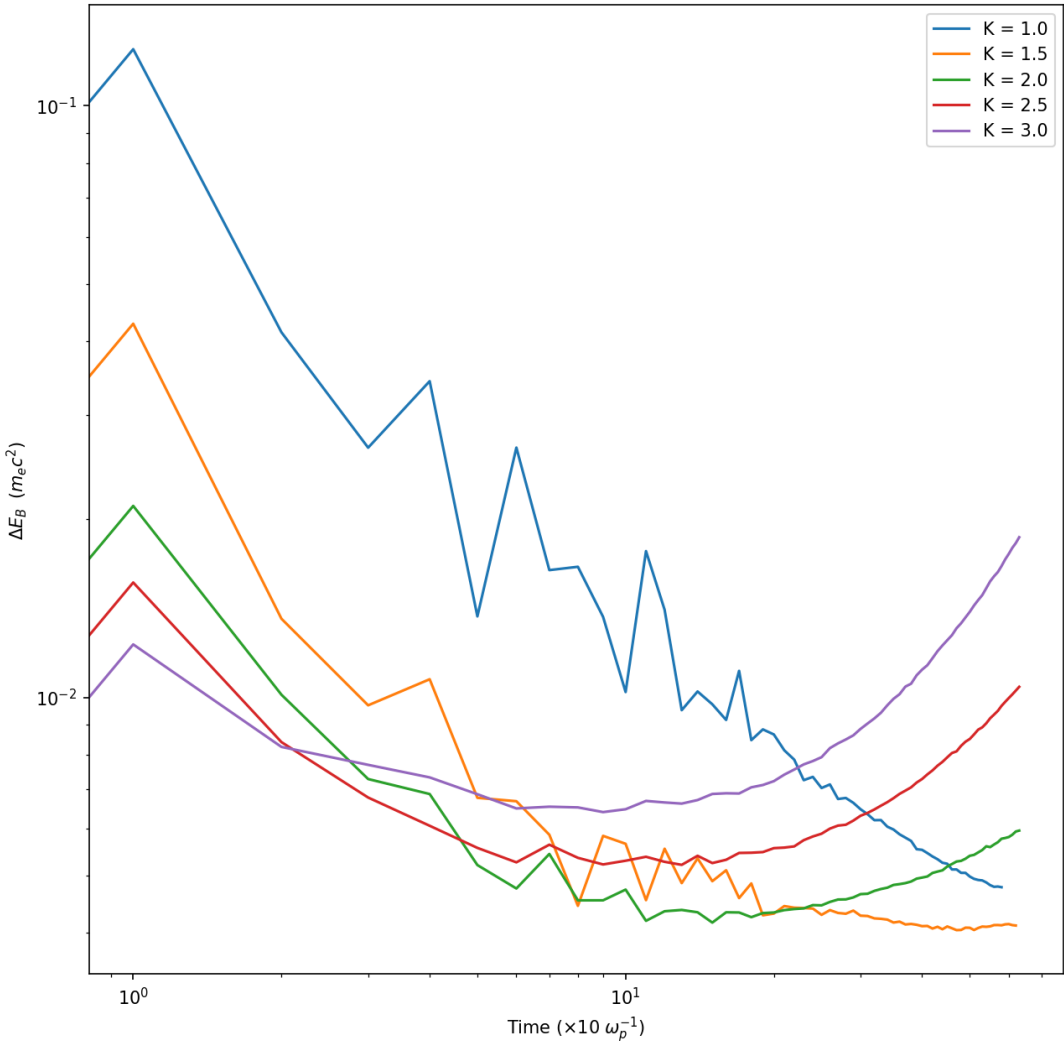


Figure 4.8: Plot of change in total electric field energy ( $\Delta E_E = E_{E,t} - E_{E,0}$ ) of the system with time ( $\times 10 \omega_p^{-1}$ ). We have illustrated here the trend for electric field energy evolution with time for all five degree of asymmetries ( $K$ ).

Since the plasma is quasi-neutral and there is no external electric field in the system at the beginning of the time step, there is not a noticeable electric energy in the system.

But we can observe that electric fields are produced in the system as it evolves as a result of reconnection. The particle acceleration is caused by these fields. It is also observed that the initially electric field is lower for higher degrees of asymmetry due to a slower rate of reconnection. However, due to particle acceleration brought on by those electric fields, electric energy is soon transferred along with the particles. Thus, we observe a sudden decline in electric energy.

#### 4.5.3 Kinetic energy

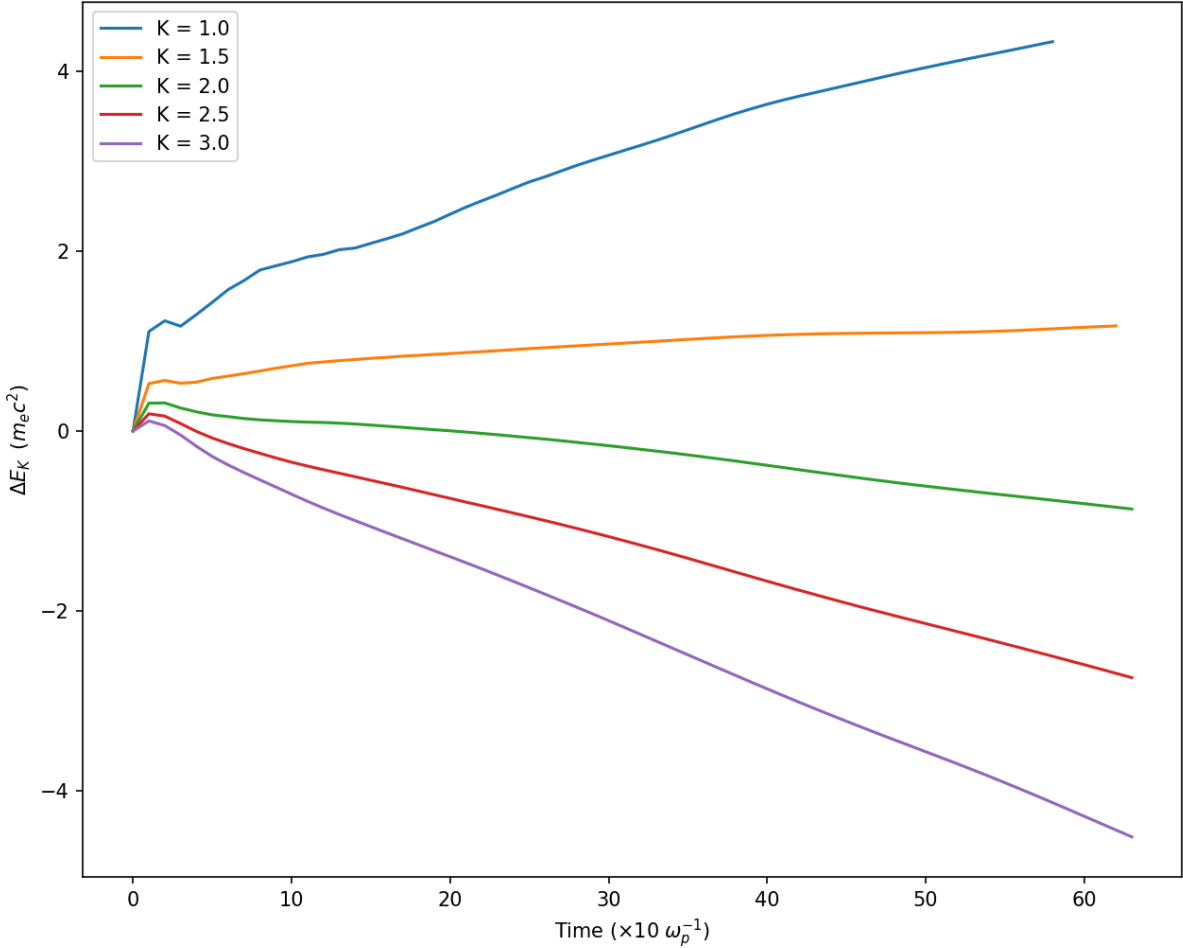


Figure 4.9: Plot of change in Total kinetic energy ( $\Delta E_K = E_{K,t} - E_{K,0}$ ) of the system with time ( $\times 10 \omega_p^{-1}$ ). We have illustrated here the trend for kinetic energy evolution with time for all five degree of asymmetries (K).

Since we have two species system so we can use following formula to calculate the kinetic energy:

$$K_{\text{electrons}} = \frac{1}{2} \sum_i m_{e,i} \mathbf{v}_{e,i}^2 \quad (4.10)$$

$$K_{\text{protons}} = \frac{1}{2} \sum_i m_{p,i} \mathbf{v}_{p,i}^2 \quad (4.11)$$

where  $m_{e,i}$  and  $m_{p,i}$  are the masses of electron  $i$  and proton  $i$ , respectively, and  $\mathbf{v}_{e,i}$  and  $\mathbf{v}_{p,i}$  are their respective velocities. The total kinetic energy for the system can then be

obtained by summing the kinetic energies for both populations:

$$K_{\text{total}} = K_{\text{electrons}} + K_{\text{protons}} \quad (4.12)$$

Upon obtaining the kinetic energy values for each time step across all five systems, we proceeded to graphically represent the data as follows. It is evident that the kinetic energy of the system experiences a noteworthy increase during its evolution for K values of 1 and 1.5. For the case where K equals 2, the observed changes are not substantial enough to infer that there is a significant occurrence of reconnection within the simulated time. However, it is noteworthy that for values of K equal to 2.5 and 3.0, a drop in kinetic energy is observed. Additional study and investigation are necessary in order to gain a comprehensive understanding of the system.

# Chapter 5

## Summary and Conclusion

The present study aimed to investigate the impact of magnetic field asymmetry on the reconnection region by conducting simulations on five distinct plasma systems. The parameters of these systems were kept constant, except for the magnetic field and particle density on one side of the reconnection region. The study involved the manipulation of magnetic field and particle density parameters to investigate their impact on the magnetic reconnection rate and energy bifurcation across all five systems.

The study involved the maintenance of a consistent magnetic field on one side of the reconnection region, while on the other side, the magnetic field was decreased by a factor of K (where K = 1, 1.5, 2, 2.5, and 3). This implies that the overall magnetic energy of the system will be reduced, resulting in an anticipated decline in the rate of reconnection. Our primary focus was to investigate whether a correlation exists between the rate of reconnection and asymmetry. The model that best fit our data was  $E_{rec,avg} = (3.606 \times 10^{-6})e^{-1.406K}$ , we also performed chi-square test and the  $\chi^2$  for this fit was  $9.27 \times 10^{-8}$  and P-value was  $\approx 1$ . As asymmetry increases, the average magnetic reconnection decreases exponentially with exponent -1.406.

As anticipated, a decrease in magnetic energy and an increase in kinetic energy were observed during the system's evolution. This is due to the conversion of magnetic energy into kinetic energy as the particle is accelerated. Subsequent to the initial abrupt decline, there is a discernible peak in magnetic energy, followed by a subsequent decline. The observed phenomenon could potentially be attributed to the amalgamation of multiple plasmoids, which subsequently accumulate and retain magnetic energy. However, as these entities coalesce to form a larger magnetic island, they discharge magnetic energy, resulting in a subsequent decline. The aforementioned statement applies similarly to the concept of kinetic energy. The acceleration of particles is observed to result in an augmentation of their kinetic energy. The phenomenon of electric energy initially exhibiting a steady increase, followed by a subsequent decline, can be attributed to the dissipation of energy during the acceleration of particles. As observed, the efficacy of the transformation of magnetic energy into kinetic energy diminishes with increasing degrees of asymmetry, as evidenced by the observed trend. The observed outcomes for K values of 2.5 and 3 exhibit a counter-intuitive pattern, which deviates from our anticipated results. To gain a comprehensive understanding of these findings, additional analysis and simulations may be necessary. Continuation of this project may represent a potential avenue for future work.

# Bibliography

- Ahedo, E., Escobar, D., Anton, A., Parra, F., and Pablo, V. (2007). Two-dimensional modelling of the hall thruster discharge: Final report. page 116.
- Bathgate, S. N., Bilek, M. M., Cairns, I. H., and McKenzie, D. R. (2018). A thruster using magnetic reconnection to create a high-speed plasma jet. *The European Physical Journal Applied Physics*, 84(2):20801.
- Birdsall, C. K. and Langdon, A. B. (1991). *Plasma Physics via Computer Simulation*.
- Birn, J. and Hesse, M. (2005). Energy release and transfer in guide field reconnection. *Journal of Geophysical Research: Space Physics*, 110(A2):A02213.
- Bittencourt, J. A. (2004). *Fundamentals of Plasma Physics*.
- Borg, A. L., Øieroset, M., Phan, T. D., Mozer, F. S., Pedersen, A., Mouikis, C., McFadden, J. P., Twitty, C., Balogh, A., and Rème, H. (2005). Cluster encounter of a magnetic reconnection diffusion region in the near-Earth magnetotail on September 19, 2003. , 32(19):L19105.
- Boris, J. P. (1970). Acceleration calculation from a scalar potential.
- Burch, J. L., Torbert, R. B., Phan, T. D., Chen, L.-J., Moore, T. E., Ergun, R. E., Eastwood, J. P., Gershman, D. J., and Cassak, P. A. (2016). Electron-scale measurements of magnetic reconnection in space. *Science*, 352(6290):aaf2939.
- Cassak, P. A. and Shay, M. A. (2012). Magnetic reconnection for coronal conditions: Reconnection rates, secondary islands and onset. *Space Science Reviews*, 172(1):283–302.
- Chen, F. (1984). *Introduction to Plasma Physics and Controlled Fusion, Volume 1: Plasma Physics*. Plenum Press.
- Comisso, L., Lingam, M., Huang, Y. M., and Bhattacharjee, A. (2016). The role of plasmoids in magnetohydrodynamic turbulence. *Physics of Plasmas*, 23(10):100702.
- Daughton, W., Roytershteyn, V., Karimabadi, H., Yin, L., Albright, B. J., Bergen, B., and Bowers, K. J. (2011). Role of electron physics in the development of turbulent magnetic reconnection in collisionless plasmas. *Nature Physics*, 7(7):539–542.
- Davidson, R. (1972). *Methods in Nonlinear Plasma Theory*. Academic Press.

- Derouillat, J., Beck, A., Pérez, F., Vinci, T., Chiaramello, M., Grassi, A., Flé, M., Bouchard, G., Plotnikov, I., Aunai, N., Dargent, J., Riconda, C., and Grech, M. (2018). Smilei : A collaborative, open-source, multi-purpose particle-in-cell code for plasma simulation. *Computer Physics Communications*, 222:351–373.
- Donkó, Z., Hartmann, P., and Kalman, G. (2007). Strongly coupled plasma liquids.
- Forbes, T. G. (2001). The nature of Petschek-type reconnection. *Earth, Planets and Space*, 53:423–429.
- Frank-Kamenetskii, D. A. (1972). *The Two-Fluid Model*, pages 59–64. Macmillan Education UK, London.
- Fried, B. (1959). Mechanism for the two-stream instability. *Physics of Fluids*, 2(3):337–342.
- Gary, S. (1993). *Theory of Space Plasma Microinstabilities*. Cambridge University Press.
- Genet Mekonnen Assefa, L. (2019). Solution of two dimensional poisson equation using finite difference method with uniform and non-uniform mesh size. *Advances in Physics Theories and Applications*.
- Gibbon, P. and Sutmann, G. (2002). Long-range interactions in many-particle simulation. *Quantum Simulations of Complex Many-Body Systems: From Theory to Algorithms*, 10.
- Hesse, M., Aunai, N., Sibeck, D., and Nakamura, R. (2014). On the electron diffusion region in planar, asymmetric, systems. *Geophysical Research Letters*, 41(23):8673–8680.
- Hoffman, J. D. (2001). *Chapter 9. Elliptic partial differential equations*. CRC Press.
- Huba, J. D. (1995). Hall magnetohydrodynamics in space and laboratory plasmas. *Physics of Plasmas*, 2(6):2504–2513.
- Konior, W. (2017). Particle-in-cell electrostatic numerical algorithm. *Transactions on Aerospace Research*, 2017(3).
- Loureiro, N. F., Schekochihin, A. A., and Cowley, S. C. (2007). Instability of current sheets and formation of plasmoid chains. *Physics of Plasmas*, 14(10):100703.
- Lui, A. T. Y., Jacquey, C., Lakhina, G. S., Lundin, R., Nagai, T., Phan, T.-D., Pu, Z. Y., Roth, M., Song, Y., Treumann, R. A., Yamauchi, M., and Zelenyi, L. M. (2005). Critical issues on magnetic reconnection in space plasmas. *Space Science Reviews*, 116(3–4):497–521.
- Mandt, M. E., Denton, R. E., and Drake, J. F. (1994). Transition to whistler mediated magnetic reconnection. *Geophysical Research Letters*, 21(1):73–76.
- N-Body, S. (2011). N-body simulation.
- Papadopoulos, K. (1988). Microinstabilities and anomalous transport. *Reviews of Geophysics*, 26(2):243–266.

- Parker, E. N. (1957). Sweet's mechanism for merging magnetic fields in conducting fluids. *Journal of Geophysical Research*, 62(4):509–520.
- Particleincell (2010). The electrostatic particle in cell (es-pic) method.
- Paul, A. (2020). Effects of a velocity shear on double current sheet systems: Explosive reconnection and particle acceleration. *arXiv preprint*.
- Priest, E. and Forbes, T. (2000a). *Magnetic Reconnection: MHD Theory and Applications*. Cambridge University Press.
- Priest, E. R. and Forbes, T. G. (2000b). Magnetic reconnection: Mhd theory and applications. *Cambridge University Press*.
- Qin, H., Zhang, S., Xiao, J., Liu, J., Sun, Y., and Tang, W. M. (2013). Why is Boris algorithm so good? *Physics of Plasmas*, 20(8):084503.
- Ren, Y., Yamada, M., Gerhardt, S., Ji, H., Kulsrud, R., and Kuritsyn, A. (2005). Experimental Verification of the Hall Effect during Magnetic Reconnection in a Laboratory Plasma. , 95(5):055003.
- Taflove, A., Hagness, S. C., and Piket-May, M. (2005). 9 - computational electromagnetics: The finite-difference time-domain method. In CHEN, W.-K., editor, *The Electrical Engineering Handbook*, pages 629–670. Academic Press, Burlington.
- Yamada, Hantao, M., Hsu, S., Kulsrud, R., Carter, T., and Zaharia, S. (1999). Magnetic reconnection with Sweet-Parker characteristics in two-dimensional laboratory plasmas. *Physics of Plasmas*, 6(5):1743–1750.
- Zhu, P. and Wesson, J. A. (1995). Plasmoids in magnetic reconnection. *Physics of Plasmas*, 2(12):4769–4776.